The large-scale properties of simulated cosmological magnetic fields

Federico Marinacci[1]⋆, Mark Vogelsberger[1], Philip Mocz[2] and Rüdiger Pakmor[3]

[1]*Kavli Institute for Astrophysics and Space Research, Massachusetts Institute of Technology, Cambridge, MA 02139, USA*
[2]*Harvard–Smithsonian Center for Astrophysics, 60 Garden Street, Cambridge, MA 02138, USA*
[3]*Heidelberger Institut für Theoretische Studien, Schloss-Wolfsbrunnenweg 35, 69118 Heidelberg, Germany*

ABSTRACT

We perform uniformly sampled large-scale cosmological simulations including magnetic fields with the moving mesh code AREPO. We run two sets of MHD simulations: one including adiabatic gas physics only; the other featuring the fiducial feedback model of the ILLUSTRIS simulation. In the adiabatic case, the magnetic field amplification follows the $B \propto \rho^{2/3}$ scaling derived from 'flux-freezing' arguments, with the seed field strength providing an overall normalization factor. At high baryon overdensities the amplification is enhanced by shear flows and turbulence. Feedback physics and the inclusion of radiative cooling change this picture dramatically. In haloes, gas collapses to much larger densities and the magnetic field is amplified strongly and to the same maximum intensity irrespective of the initial seed field of which any memory is lost. At lower densities a dependence on the seed field strength and orientation, which in principle can be used to constrain models of cosmic magnetogenesis, is still present. Inside the most massive haloes magnetic fields reach values of $\sim 10 - 100 \ \mu$G, in agreement with galaxy cluster observations. The topology of the field is tangled and gives rise to rotation measure signals in reasonable agreement with the observations. However, the rotation measure signal declines too rapidly towards larger radii as compared to observational data.

Key words: magnetic fields – MHD – methods: numerical – cosmology: theory

1 INTRODUCTION

Magnetic fields are ubiquitous in the Universe. They have been observed at all scales, ranging from planets and minor bodies in the Solar system (Vallée 1998) to galaxies (Beck & Wielebinski 2013) and clusters of galaxies (Carilli & Taylor 2002; Feretti et al. 2012). Thanks to a variety of observational techniques, present-day field intensities have been estimated for different types of objects, and measures of the polarization of radio and infrared radiation have allowed us to map the field orientation on galactic scales and beyond.

Magnetic fields also play an essential role in many astrophysical phenomena. They are an important factor for the physics of accretion on compact objects such as neutron stars and (supermassive) black holes (Balbus 2003, and references therein), where they are thought to generate relativistic jets propagating into the intracluster medium (Blandford & Znajek 1977). Propagation and diffusion of relativistic particles (i.e. cosmic rays) are heavily affected by the presence of magnetic field (e.g. Kotera & Olinto 2011).

More in general, the interaction between the field and relativistic particles provides both a mechanism for their acceleration to relativistic speeds – through the so-called Fermi (1949) mechanism – and the production of synchrotron radiation in disc galaxies (Beck et al. 2005; Beck 2007b; Berkhuijsen et al. 2003; Fletcher et al. 2011), radio-loud active galactic nuclei (AGNs; Urry & Padovani 1995, and references therein), and radio relics and haloes in galaxy clusters (Ferrari et al. 2008). On sub-galactic scales magnetic fields are one of the major components of the interstellar medium (ISM), providing a significant fraction of the pressure support needed against gravity (Boulares & Cox 1990; Cox 2005; Ferrière 2001). A vast category of stellar phenomena – for instance radiation from pulsars (Ruderman & Sutherland 1975) – is also controlled by magnetic fields. Given their widespread presence and their importance in almost any class of astrophysical objects, our theoretical understanding of the Universe is incomplete without considering magnetic fields.

Although a large amount of observational data have been collected on the existence of magnetic fields on scales up to galaxy clusters, a robust B field detection on even

⋆ E-mail: fmarinac@mit.edu

larger scales – at the level of cosmic filaments and voids – has proven to be difficult and only a few indirect constraints (Neronov & Vovk 2010), that can be also interpreted in a different framework (Broderick et al. 2012), are available. The problem in detecting B fields in such low-density environments stems from the fact that the expected field strengths are so small ($\lesssim 1\,\mathrm{nG}$) compared to those commonly found in galaxies and clusters ($\sim 10\,\mu\mathrm{G}$) such that they are at or below the detection limit of the current instrumentation, even though this should improve with the next generation of radio instruments such as SKA (Beck 2007a). The same is true for field strengths at (very) high redshift, for which only upper limits can be placed (see however Athreya et al. 1998; Bernet et al. 2008; Kronberg et al. 1992, for evidence of B field in galaxies up to $z \sim 2$).

This scarcity of data leaves us with very little observational guidance as to how magnetic fields are originally generated and subsequently amplified, a process that is also not well understood theoretically. Many models have been proposed, but these can be essentially reduced to two main scenarios. In the first scenario, seed magnetic fields are of cosmological origin and are generated by several processes during inflation, phase transitions or plasma phenomena in the early Universe (for a recent review see Widrow et al. 2012). Another alternative is represented by the so-called Biermann battery mechanism (Biermann 1950), which can operate in cosmological shocks (Ryu et al. 1998) or during reionization (Gnedin et al. 2000). Seed fields are then amplified through turbulent dynamo processes (see e.g. Arshakian et al. 2009; Federrath et al. 2011; Kulsrud et al. 1997; Schleicher et al. 2013; Sur et al. 2010), shear flows (Dolag et al. 1999) or galactic dynamos (Hanasz et al. 2004) as baryons collapse in dark matter haloes to assemble the structures that populate the Universe today.

In the second scenario, magnetic fields are produced within (proto)galaxies by stars (Pudritz & Silk 1989; Schleicher et al. 2010) and then ejected by galactic winds (Völk & Atoyan 2000; Donnert et al. 2009). Also AGN activity (e.g. Daly & Loeb 1990; Ensslin et al. 1997; Furlanetto & Loeb 2001; Beck et al. 2013a) can contribute to the generation and ejection of B fields in the intergalactic medium (IGM). The ejected field can then be amplified and dispersed by the processes described above. It is conceivable to assume that, in this second scenario, seed fields are more spatially localized near the sites where galaxies form and are then gradually dispersed by gas motions. If the dispersal process turns out to be not particularly effective, the different spatial distribution of the seed field can be used to discriminate between the two scenarios (Cho 2014).

Numerical simulations are an important tool to investigate the close link between the dynamical state of gas and the amplification of the magnetic field to the present-day strengths as cosmological structures build up. Given the importance and the vastness of the problem a number of approaches have been attempted. A possible technique is to focus on an idealized MHD setup. For instance Ryu et al. (2008, but see also Cho 2014) studied the development of MHD turbulence starting from different seed field configurations, in order to assess the amplitude of the field amplification. From this study they derive a model for injecting magnetic energy in a non-radiative cosmological simulation to recover the final magnetic field distribution.

A more attractive approach, the one considered in this paper, is to perform cosmological MHD simulations and study the amplification of the magnetic field and the growth of cosmic structures simultaneously. Although the resolution achieved is not comparable to that of idealized setups, a number of authors have performed this type of simulations focusing on a variety of spatial and mass scales.

The co-evolution of B fields and the formation of galaxy clusters have been studied by Dolag et al. (1999) in non-radiative cosmological simulations. They found that an initial B field seed is amplified by the building up of the cluster through gravitational collapse, shear flows and turbulence. The actual seed adopted has a negligible impact on the final B field strength. Those results are confirmed by subsequent studies, using a similar model but a different seeding technique, which however may affect the B field distribution in low-density regions (Donnert et al. 2009). The impact of non-ideal MHD effects has also been explored (Bonafede et al. 2011). Other authors pointed out the importance of radiative gas cooling (Dubois & Teyssier 2008) and anisotropic thermal conduction (Ruszkowski et al. 2011) in further boosting the amplification of the magnetic field and changing its orientation.

Moving to smaller scales, the emergence and the evolution of a galactic-wide magnetic field have been investigated by several works on isolated galaxies. The goals of these calculations are to clarify whether dynamo processes (Hanasz et al. 2009; Schober et al. 2012, 2013) or disc dynamics (Kotarba et al. 2009; Wang & Abel 2009) could give rise to the observed magnetic field strength in present-day Milky Way-type objects or their progenitors, and to assess the impact of the B field on galaxy properties such as their star formation history (Wang & Abel 2009; Pakmor & Springel 2013). The role of supernova-driven galactic winds in explaining the magnetization of the IGM was also considered (Dubois & Teyssier 2010). Magnetic fields in Milky Way-type galaxies have also been studied in zoom-in cosmological simulations, focusing on mechanisms for the generation of the seed magnetic field (Beck et al. 2013b) and investigating how a primordial seed field is amplified in the halo surrounding the central galaxy (Beck et al. 2012) or within the galaxy itself (Pakmor et al. 2014). In particular, Pakmor et al. (2014) showed that it is possible to form a realistic disc galaxy with a well-defined morphology and simultaneously predict the observed magnetic field strength and orientation of late-type systems.

While there are many example of MHD calculations on galactic and galaxy cluster scales, global cosmological simulations (i.e. uniformly sampled boxes) are relatively rare in the literature. A notable exception, which however includes only adiabatic physics and treats other physical processes such as particle acceleration in post-processing, is presented by Vazza et al. (2014, 2015b), who performed high-resolution static-mesh simulations (up to 2400^3 grid and $300\ h^{-1}\mathrm{Mpc}$ box sizes) to study the small-scale dynamo in a cosmological volume. Another interesting forthcoming project is the MAGNETICUM simulation suite (Dolag et al., in preparation), which will include B fields with the scheme described by Dolag & Stasyszyn (2009).

In the present study, we aim at pushing forward the modelling of uniformly sampled cosmological simulations by including magnetic fields – through the ideal MHD approx-

imation – in a series of calculations performed with the moving-mesh code AREPO (Springel 2010). Our goal is to study the general properties of cosmological magnetic fields and their variation as a function of resolution, seed field and baryon physics. To this end we perform two sets of simulations at different resolution levels: one set only including adiabatic gas physics; the other featuring the fiducial model of baryon physics of the ILLUSTRIS simulation (Vogelsberger et al. 2014a,b). To our knowledge, this is the first time that a successful physics model including the most important processes for galaxy formation is used in this type of simulations. The paper is organized as follows. In Section 2 we describe the numerical methodology that we adopted both to generate the initial conditions (ICs) and to run the simulations. In Section 3 we present the main findings of our simulations, which include the large-scale properties of the magnetic field (Sec. 3.1), their dependence on the choice of the seed field strength (Sec 3.2), the properties of B field within haloes (Sec. 3.3), and Faraday rotation measure (RM) predictions (Sec 3.4). In Section 4 we discuss our results, while Section 5 gives our conclusions.

2 NUMERICAL METHODOLOGY

To study the amplification of magnetic field and its properties in a cosmological context, we run a series of ideal MHD simulations of uniformly sampled cosmological boxes of size $100\,h^{-1}$Mpc. We repeat the simulations for two different resolution levels with a total particle number of 2×256^3 and 2×512^3, respectively. Each configuration is simulated twice: one time by just considering adiabatic physics, a second time by including the most important physical processes for galaxy formation. The main properties of the runs can be found in Table 1.

We adopt the set of cosmological parameters according to the re-analysis of *Planck* data performed by Spergel et al. (2015, table 3). This features a Λ cold dark matter (ΛCDM) cosmology with parameters $\Omega_{\rm m} = 0.302$, $\Omega_{\rm b} = 0.04751$, $\Omega_\Lambda = 0.698$, $\sigma_8 = 0.817$, $n_{\rm s} = 0.9671$, and a Hubble parameter $H_0 = 68$ km s^{-1}Mpc^{-1} (hence implying $h = 0.68$). We compute the transfer function for this cosmology with CAMB (Lewis & Bridle 2002), and generate the ICs with MUSIC (Hahn & Abel 2011). The ICs are created for dark matter simulations only at a starting redshift of $z = 127$ and baryons are introduced at the beginning of the simulation through the procedure described in Marinacci et al. (2014a,b).

We evolve the ICs created above with the moving-mesh cosmological code AREPO (Springel 2010), complemented with the extension to include ideal MHD developed by Pakmor & Springel (2013) and successfully applied in 'zoom-in' cosmological simulations of (individual) disc galaxies (Pakmor et al. 2014). We refer the reader to the original papers for an exhaustive description of the code and for all the details about the implementation of its modules. Here, we give just a brief overview of the most important code features.

AREPO solves gravitational and collision-less dynamics via a standard TreePM method (also used, by the popular GADGET-2 code; Springel 2005), that splits the gravitational force in a long-range contribution, computed by a Fourier transform method on a mesh, and a short-range

contribution, calculated by an oct-tree algorithm (Barnes & Hut 1986). For (ideal) MHD, AREPO adopts finite-volume discretization on an unstructured Voronoi tessellation of the simulation volume. MHD equations are solved through a second-order MUSCL-Hancock scheme (e.g., Toro 1999) coupled to the approximate HLLD Riemann solver (Miyoshi & Kusano 2005). The Voronoi mesh is free to move with the local fluid velocity field. This results in a manifestly Galilean-invariant, quasi-Lagrangian numerical method that keeps the mass per gas cell approximately constant.

To ensure the $\nabla \cdot \boldsymbol{B} = 0$ constraint the MHD module currently employs the divergence cleaning technique developed by Powell et al. (1999). We are aware of the fact that this technique cannot guarantee $\nabla \cdot \boldsymbol{B}$ identically vanishing throughout the simulation domain but our scheme has proven to yield acceptable divergence errors and results of the same quality as compared to constrained transport (CT) schemes (Pakmor & Springel 2013). Nevertheless, we are working to include a CT scheme in AREPO, based on the approach described by Mocz et al. (2014), to use it in future simulations and to address the potential shortcomings of the Powell et al. (1999) method (see Hopkins & Raives 2015, and references therein).

In ideal MHD simulations it is not possible to generate a magnetic field starting from zero-field ICs. Therefore, the magnetic field must be seeded appropriately. For simplicity, we seed a homogeneous magnetic field in the box at the starting redshift along a prescribed direction. This ensures a divergence-free initial B field, but leaves us with two parameters to be chosen: the initial field strength and direction. Previous zoom-in cosmological MHD simulations with AREPO (Pakmor et al. 2014) have shown that the final results are rather insensitive to the choice of these parameters, at least at high overdensities. We will explore the situation at lower overdensities in Section 3.2.

Our simulation set also includes a comprehensive model for galaxy formation physics (Vogelsberger et al. 2013) specifically developed for the ILLUSTRIS simulation suite (Vogelsberger et al. 2014b,a). The model was calibrated against a small set of key observables, such as the cosmic star formation history and the galaxy stellar mass function, and it is able to successfully reproduce most of the observed properties of the global galaxy population at redshift zero. A detailed description of all the components of the model can be found in Vogelsberger et al. (2013) and its integration within the AREPO MHD module in Pakmor et al. (2014). In our runs we use the same fiducial settings as in Vogelsberger et al. (2013).

Finally, we want to note that in our simulations diffusive effects – which are important to determine the level of turbulence at small scales and the level of B field amplification through dynamo mechanisms – are controlled by the numerical cutoff scale. Therefore, we expect the magnetic Reynolds number to be of the same order of the Reynolds number, implying a magnetic Prandtl number of $\sim O(1)$ (Federrath et al. 2011). The Reynolds number in halo of virial radius r_{200} can be estimated in our runs as (see Vazza et al. 2014)

$$\mathrm{Re} \approx \left(\frac{r_{200}}{\Delta x}\right)^{4/3} = \left(\frac{M_{200}N^3}{\Omega_m \rho_{\rm crit}L^3}\right)^{4/9}, \qquad (1)$$

where Δx is the typical size of the resolution element inside

Simulation	$N_{\rm tot}$ (DM + cells)	$M_{\rm DM}$ $(10^5\,h^{-1}{\rm M}_\odot)$	$M_{\rm gas}$ $(10^5\,h^{-1}{\rm M}_\odot)$	Box size $(h^{-1}{\rm Mpc})$	ϵ $(h^{-1}{\rm kpc})$	B_0 (G)
box-256-ad	2×256^3	4.21×10^4	7.86×10^3	100	5.0	$(0, 0, 10^{-14})$
box-512-ad	2×512^3	5.26×10^3	9.82×10^2	100	2.5	$(0, 0, 10^{-14})$
box-256-ad-low	2×256^3	4.21×10^4	7.86×10^3	100	5.0	$(0, 0, 10^{-16})$
box-512-ad-low	2×512^3	5.26×10^3	9.82×10^2	100	2.5	$(0, 0, 10^{-16})$
box-256-ad-high	2×256^3	4.21×10^4	7.86×10^3	100	5.0	$(0, 0, 10^{-12})$
box-512-ad-high	2×512^3	5.26×10^3	9.82×10^2	100	2.5	$(0, 0, 10^{-12})$
box-256-fp	2×256^3	4.21×10^4	7.86×10^3	100	5.0	$(0, 0, 10^{-14})$
box-512-fp	2×512^3	5.26×10^3	9.82×10^2	100	2.5	$(0, 0, 10^{-14})$
box-256-fp-low	2×256^3	4.21×10^4	7.86×10^3	100	5.0	$(0, 0, 10^{-16})$
box-512-fp-low	2×512^3	5.26×10^3	9.82×10^2	100	2.5	$(0, 0, 10^{-16})$
box-256-fp-high	2×256^3	4.21×10^4	7.86×10^3	100	5.0	$(0, 0, 10^{-12})$
box-512-fp-high	2×512^3	5.26×10^3	9.82×10^2	100	2.5	$(0, 0, 10^{-12})$
box-256-ad-ydir	2×256^3	4.21×10^4	7.86×10^3	100	5.0	$(0, 10^{-14}, 0)$
box-256-fp-ydir	2×256^3	4.21×10^4	7.86×10^3	100	5.0	$(0, 10^{-14}, 0)$

Table 1. Properties of the performed simulations. Each box is simulated two times: the first time considering only adiabatic physics and the second including the most important physical processes for galaxy formation. Columns give (from left to right): simulation name, total number of dark matter particles plus gas cells, mass resolution in the dark matter component, mass resolution in the gas component, simulation box size, maximum physical gravitational softening (reached at $z = 1$), and initial (comoving) seed magnetic field.

the halo, M_{200} is the halo viral mass, N^3 is the total number of resolution element in the box, L is the box size, $\Omega_{\rm m}\rho_{\rm crit}$ is the total matter density in the Universe, and the last equality holds because gas is discretized in volume elements having roughly the same mass (see also Sect. 4). We have implicitly assumed that the halo contains all the baryons associated with its dark matter halo. For $N = 512$, equation (1) yields Re ≈ 100 for a halo of $\simeq 10^{13}\,{\rm M}_\odot$ and Re ≈ 500 for a halo of $\simeq 10^{15}\,{\rm M}_\odot$, respectively. While these value are somewhat lower than those achieved in more idealized setups (Sur et al. 2010, 2012) or cosmological simulations (Vazza et al. 2014), they are nevertheless in the regime in which a small-scale dynamo can be in operation (Schekochihin et al. 2004).

3 RESULTS

3.1 Large-scale properties of the magnetic field

We start the analysis of our simulations by presenting the general large-scale properties of the resulting field. In Fig. 1, we show mass-weighted projections of the B field intensity[1] at different redshifts for the simulations box-512-ad (left) and box-512-fp (right). The intensity and direction of the seed field are the same for the two simulations and the latter coincides with the projection axis. The projections are obtained by considering a region extending the full size of the computational domain (100 h^{-1}Mpc in comoving units) perpendicularly to the projection axis for a thickness of 50 h^{-1}Mpc (again in comoving units). The centre of the projection region coincides with that of the computational domain.

The B field evolution traces the distribution of matter in both simulations. The largest values of the magnetic field are located at the density peaks. This is expected, since in ideal

MHD the flux of the B field is conserved. Therefore, density peaks are expected to host the largest B field, while in voids, where the cosmological expansion is dominant, the smallest values of the B field can be found. We recall that in the case of adiabatic (and homogeneous) contraction/expansion flux conservation dictates that the magnetic field evolves as

$$\boldsymbol{B} = \frac{\boldsymbol{B_0}}{a^2} \propto \rho^{2/3}, \qquad (2)$$

where $a = (1 + z)^{-1}$ is the cosmological scale factor, $\boldsymbol{B_0}$ is the rescaled intensity of the B field at $z = 0$, and ρ is the gas density. Equation (2) shows that the net effect of cosmic expansion is a decrease in the physical intensity of the B field, clearly visible in the late redshift panels of Fig. 1 in underdense regions.

The magnetic field in the full physics simulation can reach much higher values at the centres of massive haloes. Here the B field reaches intensities that are several orders of magnitude greater than in the adiabatic case (see e.g. Fig. 4). The main cause for this is the inclusion of radiative cooling and feedback loops (galactic winds and AGN feedback) in the simulations. Radiative cooling allows gas to reach higher densities than in the adiabatic case, which in turn boost the amplification of the B field because of flux conservation. Also, the presence of gas outflows due to stellar and AGN feedback make the halo environment more 'violent' increasing the importance of turbulence and shear flows, which again boost the amplification of the B field. The values of the B field between the two simulations tend to increase with time. At high redshift ($z = 2$) the projections look very similar, but as time goes on and the assembly of the cosmic structure progresses the differences become more marked. Although the morphology of low-density regions and in voids in particular is similar in both simulations, the B field strength is somewhat larger with the inclusion of baryon physics since stellar and AGN feedback can eject highly magnetized gas from the centres of haloes in the intergalactic space.
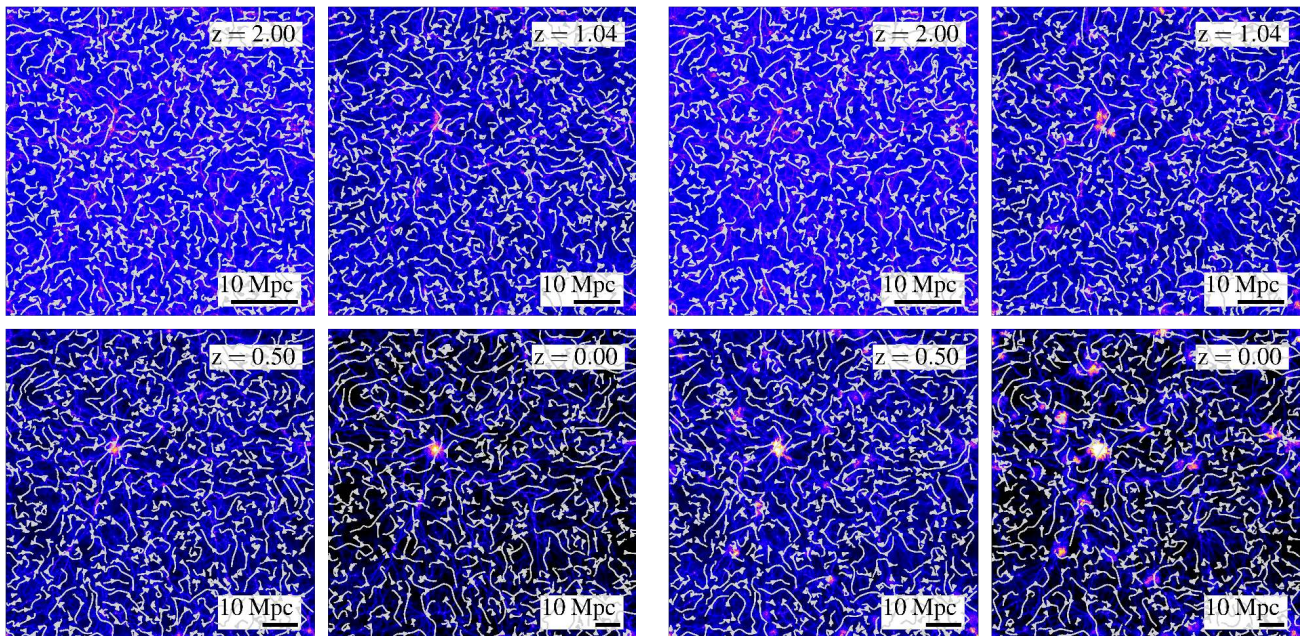
Fig. 2 displays a two-dimensional slice through the cen-

[1] Unless otherwise stated, the values of magnetic field shown in the figures are always the physical ones.
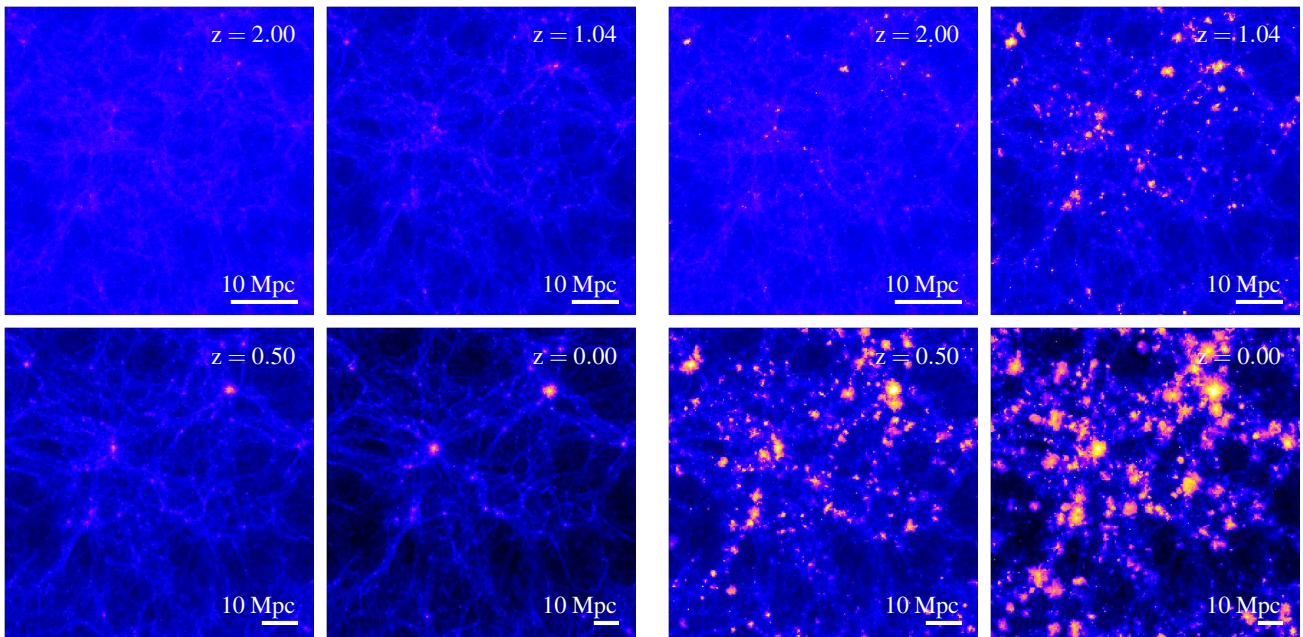
Figure 1. Mass-weighted projection of the intensity of the B field at different redshifts, as indicated in the top-right corner of each panel, for the simulation box-512-ad (left) and box-512-fp (right). Each panel is 100 h^{-1}Mpc on a side (in comoving units), the full extent of the simulated box. The centre of the projection region corresponds to that of the simulated domain. The plots have been obtained by considering all the gas cells along the z-axis (the initial direction of the seed field) within 25 h^{-1}Mpc (in comoving units) from the centre, for a total thickness of 50 h^{-1}Mpc. The physical scale at the corresponding redshift is indicated on the bottom-right corner of each panel. The colour scheme is the same for all the panels and maps logarithmically magnetic field intensities in the interval $[10^{-9}, 10^{-2}]\,\mu$G.

.

Figure 2. Slice through the centre of the simulated box of the B field intensity at different redshifts, as indicated in the top-right corner of each panel, for the simulation box-512-ad (left) and box-512-fp (right). Each panel is 100 h^{-1}Mpc on a side (in comoving units), the full extent of the simulated box. The over plotted magnetic field lines show the direction of the B field on to the slice plane. The colour scheme is the same for all the panels and maps logarithmically magnetic field intensities in the interval $[10^{-9}, 10^{-3}]\,\mu$G.
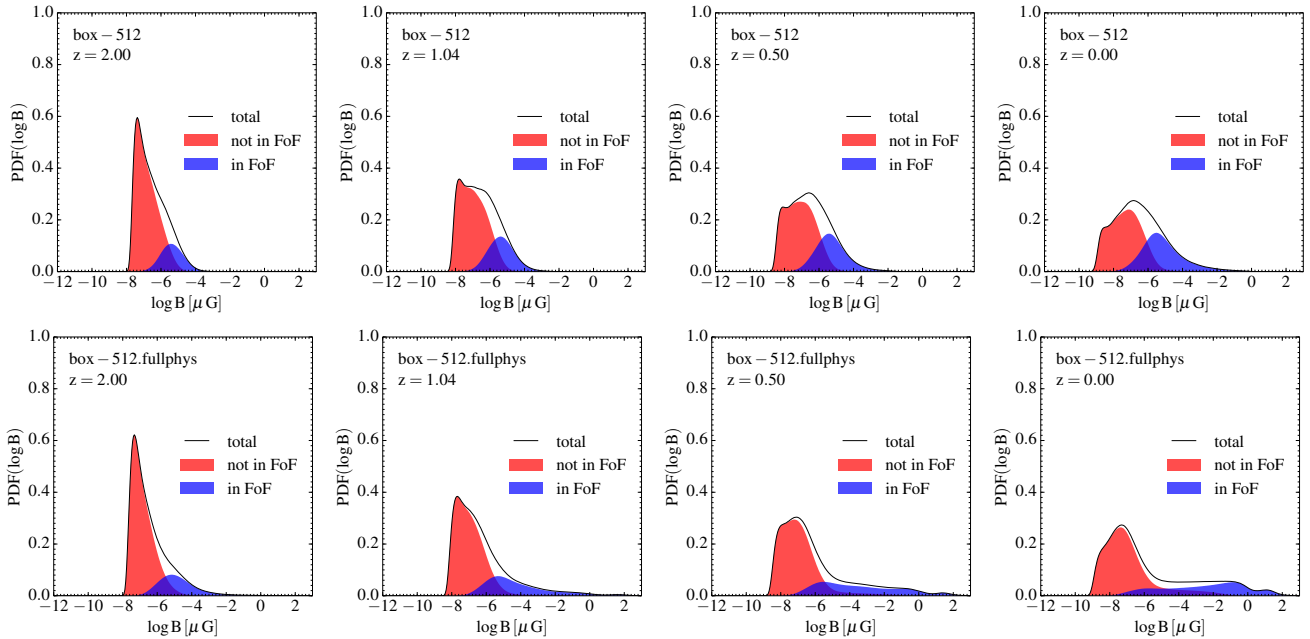
Figure 3. Redshift evolution of the B field PDF for the simulation box-512-ad (top) and box-512-fp (bottom). Redshift is indicated on the top-left corner of each panel. The colour shading shows the contribution to the total PDF (black solid line) of gas cell in FOF-identified structures (blue) and not in FOF groups (red). The growth of cosmic structures can be clearly seen in the panels as the contribution to the B field PDF of gas cells not in FOF groups decreases in favour of that comprising FOF groups. The growth of cosmic structures – together with baryon physics effects in the full physics run – also drives the amplification of B field, visible as a more pronounced tail in the PDF at high B field intensity at late times. Moreover, the expansion of the Universe can be detected as a shift of the peak in the PDF of gas cells not contained in FOF groups towards lower values for decreasing redshift.

tre of the simulated domain in a direction perpendicular to the z-axis of the B field intensity for the simulations box-512-ad (left) and box-512-fp (right). The layout of the figure is the same as Fig 1, and the colour mapping has been kept the same for both simulations. To give an idea of the orientation of the magnetic field on to the slice plane we overplot magnetic field lines, with a small arrow indicating the field direction. At late times the largest B fields are found in the largest structure that is visible in the slice. A mild magnetic field strength enhancement is present also in the filaments that surround the main halo, while in voids, due to the cosmological expansion, the physical B field strength decreases at redshift zero to the value of the initial seed field or below.

Except for the densest regions (i.e. the main halo forming in the slice) the evolution of the magnetic field is essentially the same in the two simulations. Even the direction of the field is very similar, as the overplotted field lines show. This reinforces the idea that baryon physics has a fundamental role for the amplification of the B field, but this role is limited to up to cluster scales. On larger scales, gravitational dynamics and cosmological expansion alone set the final field configuration.

In Fig. 3 we present the redshift evolution of the magnetic field probability density function (PDF) for the reference simulations box-512-ad (top row) and box-512-fp (bottom row). For each B field PDF the relative contribution of gas cells contained (blue shading) and not contained (red shading) in friends-of-friends (FOF) groups is shown. This division roughly separates scales where baryonic effects are expected to have a strong impact on the B field amplifica-

tion from those where gravitational dynamics and cosmic expansion dominate, instead.

From Fig. 3 it is readily apparent that the formation and growth of cosmic structures as a function of time lead to a decrease of the peak of the PDF at low B field values. Almost all the contribution to this peak comes from gas cells not contained in FOF groups. As time passes and more and more cells are incorporated into gravitationally collapsed objects the height of this feature decreases, partially compensated by an increase of the contribution to the total PDF from particles included in FOF groups. However, the peak at low values of B field never completely disappears, even at redshift zero. The width of the B field PDF of gas cells not included in any structure broadens with time. Here, two effects are at work: the cosmological expansion, that tends to lower the B field and detectable as a movement of the left edge of the PDF with decreasing redshift, and the amplification of the B field in intermediate-density regions such as filaments, that tend to move gas cells towards higher B field values. This behaviour is the same in both simulations. Indeed the shape of the non-FOF part of the B field PDF and its evolution are remarkably similar in both runs.

The situation changes significantly for the B field PDF of gas cells contained in FOF groups. The evolution of this part of the PDF is markedly different for the two runs. There is a general trend of an increase of the relative contribution of this part to the total PDF as a function of time for both simulations, which can be readily explained by the growth of cosmic structures driving the magnetic field amplification. Another common feature is the formation of a peak at $\approx 10^{-6}\,\mu$G. In the adiabatic case the amplitude of this peak
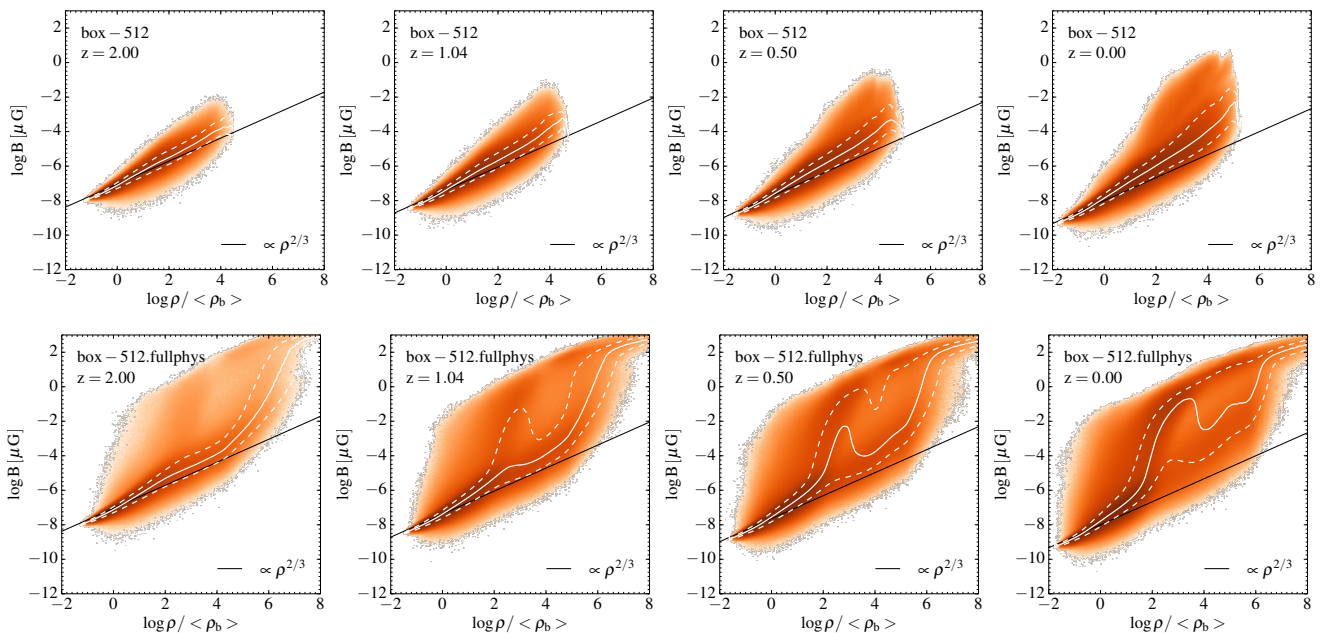
Figure 4. Redshift evolution of the B field intensity versus baryon overdensity for the simulation box-512-ad (top) and box-512-fp (bottom). Redshift is indicated on the top left corner of each panel. The panels show two-dimensional histograms colour coded according to the mass of gas falling on to each bin (darker shades correspond to larger masses). White lines represent the median (solid) and the 16th and 84th percentiles (dashed) of the B field distribution as a function of the baryon overdensity. The black solid line is the expected density scaling of the B field intensity ($\propto \rho^{2/3}$) based on the flux conservation. For decreasing redshift is clearly visible how the assembling of cosmic structures (here represented by the increase of the dynamic range in overdensities with decreasing redshift) drives the amplification of the B field. At high redshift the median relation essentially corresponds to the scaling $\propto \rho^{2/3}$ expected from flux freezing, but it steepens at later time and towards higher overdensities indicating a boost in the B field amplification due to structure formation. In the full physics case the amplification is further enhanced by radiative cooling and stellar and AGN feedback. Also noticeable is the effect of the cosmological expansion as a reduction of the overall B field normalization $\propto (1+z)^2$ with decreasing redshift.

slowly but steadily increases with time, and the contribution to the total PDF is symmetric with respect to the peak location. The maximum magnetic field intensity, however, rarely exceeds $\approx 10^{-2}\,\mu$G. In the full physics simulation the formation of the peak at $\approx 10^{-6}\,\mu$G is still visible, but its amplitude is lower and the contribution to the total PDF more skewed towards higher values of B field intensity at all redshifts. At redshift zero this feature disappears and a bump forms at $\approx 1\,\mu$G. The maximum value of the B field intensity reached at the end of the simulation is $\approx 10^2\,\mu$G, about four orders of magnitude larger than in the adiabatic case. This demonstrates that the full spectrum of baryon physics is necessary to amplify primordial magnetic fields to the values ($\sim 10-100\,\mu$G) that are observed in galaxies and galaxy clusters at low redshifts (e.g. Carilli & Taylor 2002; Basu & Roy 2013; Beck et al. 1996; Beck & Wielebinski 2013; Feretti et al. 2012, and references therein).

In Fig. 4 we present two-dimensional histograms of B field intensity versus baryon overdensity ($\rho/\langle\rho_b\rangle$ where the latter term is the mean baryon density) at different redshifts for the reference runs box-512-ad (top row) and box-512-fp (bottom row). The colour shading in the histogram represents the gas mass falling on to each bin. We also overplot the trends of the 16th, median and 84th percentiles (white lines) plus the scaling $\propto \rho^{2/3}$ (see also eq. [2]) expected from magnetic flux conservation (black line).

In the adiabatic case, a well-defined relation exists be-

tween the B field strength and baryon overdensity. This relation is indicative of the fact that magnetic field amplification and mass assembly in cosmic structures are tightly linked. The degree of scatter increases with overdensity, as shown by the diverging behaviour of the 16th and 84th percentile with respect to the median relation, suggesting that at high overdensities some other mechanism (i.e. turbulence and shear flows) other than gravitational collapse is at work to boost the magnetic field strength. This idea is further supported by the steepening of the median relation with respect to the scaling expected by magnetic flux conservation ($\propto \rho^{2/3}$) as a function of time. The latter describes well the intensity of the B field at low overdensities, but underpredicts its median strength in the most dense regions.

These general trends can also be observed in the full physics simulation. However, when the histograms are compared, the difference in dynamic range in both overdensity and magnetic field intensity with respect to the adiabatic case is immediately noticeable. Due to the inclusion of radiative cooling, the baryon overdensity can reach values as high as 10^8, almost three orders of magnitude larger than in the previous case. The effect on the magnetic field strength is also dramatic: at $z=2$ for overdensities $\gtrsim 10^3$ bins at B field strength $\gtrsim 1\,\mu$G are already populated. Eventually, a second branch in the relation at high B field forms, which is shifted from the prediction of magnetic flux conservation by $\sim$ five to six orders of magnitude. The larger overden-
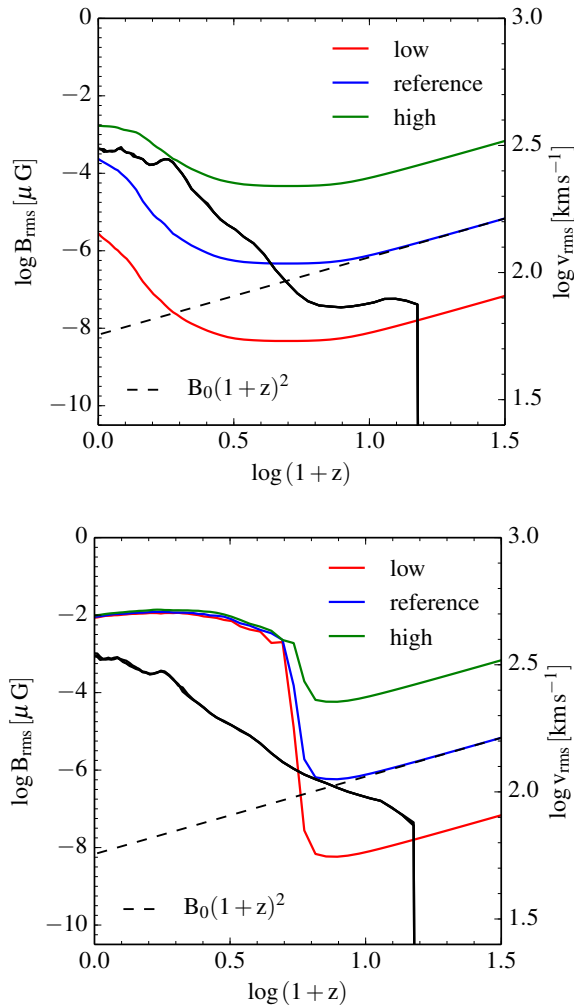
Figure 5. Evolution of the rms velocity (black solid line) and the volume-weighted B field rms (coloured lines) as a function of redshift in the box-512-ad (top) and box-512-fp (bottom) simulations. Both calculations are repeated with different initial seed field strengths, as indicated in the legend. The black dashed lines show the B field evolution due to the Universe expansion under the assumption of (global) magnetic flux conservation.

sity range caused by gas cooling is not the only reason for such a strong enhancement of the B field intensity with respect to the previous simulation, as the upper branch of the histogram starts at overdensities of $\sim 10^3$, well within the reach of the adiabatic run. Therefore, the combination of radiative cooling and larger shear flows and turbulence caused by galactic outflows (which are powered by stellar and AGN feedback) is necessary to explain the high degree of amplification of the magnetic field in the full physics case.

3.2 Dependence on the strength of the seed field

The seed field in our simulations can arbitrarily be chosen and there are different seeding strategies that have been adopted in numerical simulations, also depending on the scales of the simulated problem (see e.g. Dolag et al. 1999; Donnert et al. 2009; Dubois & Teyssier 2010; Hanasz et al.

2009; Kotarba et al. 2009). The only stringent constraint is that the seeding strategy must yield a divergence-free initial field. In our runs we adopted the simplest approach: a uniform field throughout the simulation box. This approach leaves us the freedom to select the intensity of the initial seed field and its direction as well. The present section is devoted to study how the properties presented in Sect. 3.1 vary as a function of the initial field intensity. We find that the orientation of the seed field has a smaller impact on the final simulation results, and we defer the discussion of this aspect to Sect. 4.

In Fig. 5, we show the evolution of the root mean square volume-weighted B field – a measure of the total magnetic energy – in the whole simulation box as a function of redshift for the reference (i.e. 2×512^3) adiabatic simulation (top panel) and the its full physics counterpart (bottom panel). To investigate the effects of the seed field strength, we repeat each calculation three times with different intensities of the initial seed field. In our fiducial setting (blue lines) the initial seed field strength is $||\boldsymbol{B}_0|| = 10^{-14}$ G. We then explore two additional configurations with $||\boldsymbol{B}_0|| = 10^{-16}$ G (red lines) and $||\boldsymbol{B}_0|| = 10^{-12}$ G (green lines), for a total variation in the initial magnetic field intensity of four orders of magnitude. The black dashed line in each panel is a guiding line that shows the evolution of the B field intensity (in the case of our fiducial set up) only due to the expansion of the Universe under the assumption of (global) magnetic flux conservation.

The B field evolution at high redshift is very similar in both the adiabatic and the full physics case, and is largely dominated by the expansion of the Universe, with the different intensities of the seed field accounting for an overall normalization factor. At about $z \approx 3$ structure formation leads to deviations from this simple trend, and a clear upturn of the field intensity can be observed. Turbulence and shear flows induced by structure formation are the primary mechanisms by which the field is amplified then. The late time evolution, however, is markedly different. The major difference is of course the final level of amplification reached in the two cases, with the full physics simulations reaching a final value of the B field strength that is at least ~ 10 times larger than in the adiabatic case. The other striking difference is that in the full physics runs the final amplitude of the B field ($\sim 10^{-2} \, \mu$G) is reached *regardless* of the initial seed field intensity (i.e. the amplification process *saturates* [2] after $z \approx 2$), while in the adiabatic simulation this is not the case and the evolution curves are merely a rescaled version (with the initial seed field giving again an overall normalization factor) of one another. The only effect of changing the initial seed field intensity in the full physics run is a minimal delay (for decreasing seed fields) of the time at which the exponential amplification from the (global) flux-conserving evolutionary phase to the final B field values saturates (see also Pakmor et al. 2014). A fit to the exponential amplification phase results into an e-folding

---

[2] In this work with saturation we indicate this independence of the final field strength from the initial value of the seed field intensity, or that at a fixed overdensity the magnetic field is amplified to a maximum value that depends only on the overdensity but not on the seed field strength (see also Figs 6 and 7).
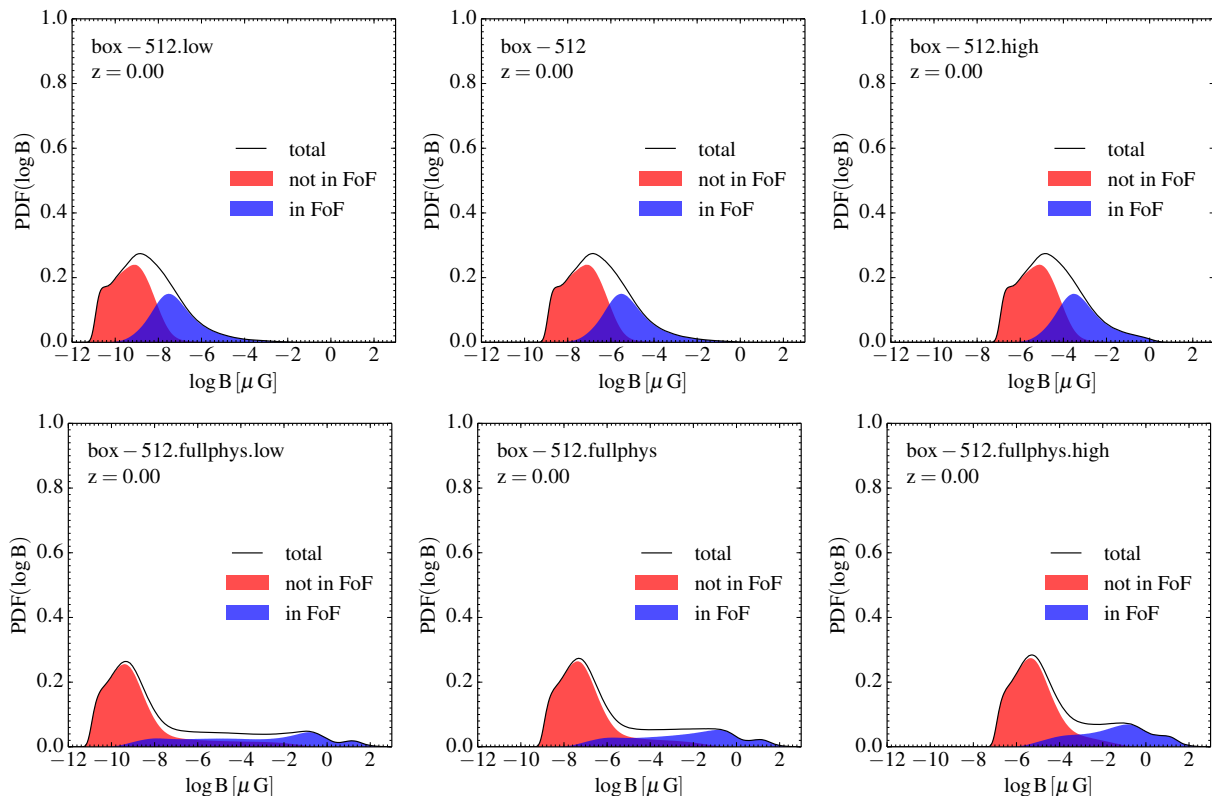
Figure 6. B field PDF at redshift zero for the simulations box-512-ad (top row) and box-512-fp (bottom row) with varying initial B seed field strength. The initial field strength is 10^{-16}, 10^{-14} and 10^{-12}G from left to right. The panels show the relative contribution to the total PDF (black line) of gas cells not contained in any of the FOF groups (red shading) and included in FOF structures (blue shading). The B field PDF is essentially unaffected by a change in the initial value of the seed field, except for a global rescaling of the B field strength visible as a horizontal shift of the plots in each row.

time for $B_{\rm rms}$ of $\simeq 0.1$, 0.14, 0.23 Gyr from the lowest to the highest seed field strength.

The black solid lines in both panels display the redshift evolution of the gas rms velocity $v_{\rm rms}$ for all cells in FOF groups. The bulk velocity of the FOF groups has been subtracted from gas particles before computing $v_{\rm rms}$, so that this quantity can be thought as a rough measure of gas turbulent motions. For each panel we plot the evolutionary tracks of $v_{\rm rms}$ for different seed fields, which however are practically indistinguishable from one another. This agrees with the findings of Sect. 3.3 in which we show that magnetic fields are not dynamically important even within haloes where their strength is the largest. $v_{\rm rms}$ increases with decreasing redshift in both adiabatic and full-physics simulations. The $v_{\rm rms}$ values reached in the full-physics runs are larger than in their adiabatic counterparts at all redshifts. This is consistent with the picture discussed in the previous section in which feedback-induced galactic outflows are an important source of shear and turbulent gas motions that in turn promote magnetic field amplification.

In Fig. 6, we show how the redshift zero B field PDF is affected by the choice of the initial field strength for the two reference simulations box-512-ad (top row) and box-512-fp (bottom row). In each row the seed field initial strength increases from left to right. The meaning of the shaded areas is the same as in Fig. 3.

In the adiabatic run, it is readily apparent that the

shape of the B field PDF and those of the contributions of gas cells in structures and outside them is essentially unchanged for the three different choices of the seed field. Only the PDF position along the x-axis varies, and in particular it shifts by two orders of magnitude in each panel. This is the exact value by which the seed field is varied in each configuration. Thus, we conclude again that the initial intensity of the seed field in the adiabatic run just sets the overall normalization of the final magnetic field. From this follows that the B field in the adiabatic runs is on global scales dynamically unimportant – at least for the intensity range explored here. As far as the intensity of the B field is concerned, the amplification factor due to gas and gravitational dynamics is not affected by the initial field strength: the final maximum intensity values are different but their *ratio* with the seed field strength is the same.

The behaviour of the B field PDF in the full physics run is slightly more complex. Here, in fact, there is a difference between low-value and high-value B field parts. The low B field part, mostly comprised by gas cells not part of any FOF group, is almost identical to its adiabatic counterpart and exhibits the same shift along the x-axis as a function of the seed field strength. The high B field part has a different behaviour. First of all, the largest values that the B field can reach are almost independent of the initial seed field strength, meaning that the amplification process has reached saturation. Note that this result agrees with what found by
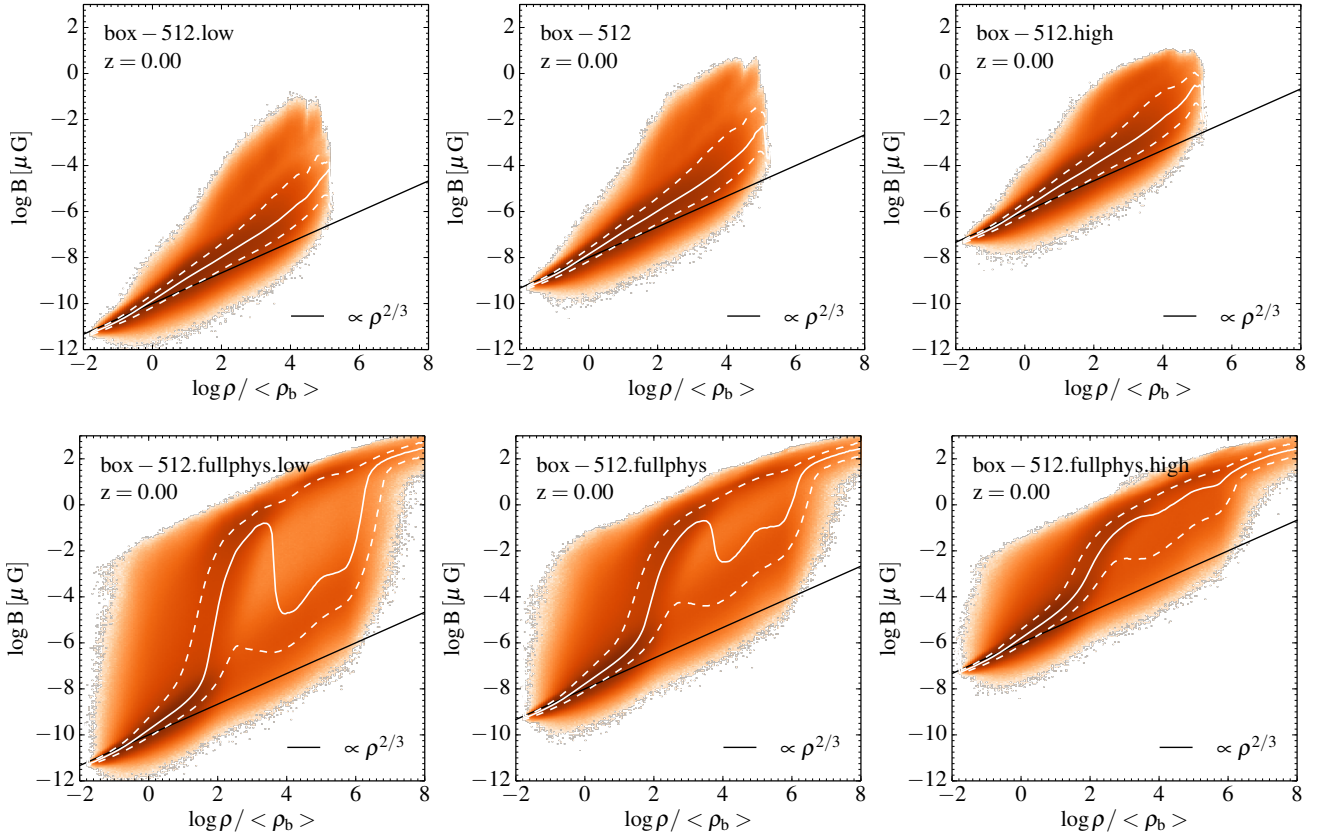
Figure 7. *B* field versus baryon overdensity at redshift zero for the simulations box-512-ad (top row) and box-512-fp (bottom row) as a function of the initial *B* seed field strength. The initial field strength is 10^{-16}, 10^{-14} and 10^{-12}G from left to right. The meaning of the colour scale and of the lines in each panel is the same of Fig. 4. For the adiabatic run there is essentially no change in the relation except a global rescaling of the *B* field strength due to the variation of intensity of seed field visible as a global vertical shift of the plot in the three panels. The same scaling is present also in the full physics run for low magnetic field intensities. However, the region of the plot at higher *B* field values is unaffected by the choice of the seed field, signalling that in those regions saturation is reached.

Pakmor et al. (2014), who explored an even larger range of seed fields in 'zoom-in' MHD simulations of disc galaxy formation with AREPO. Since the largest *B* values are fixed as a function of the seed field, the contribution of particles in FOF structures to the total *B* field PDF has a different shape in three panels, with a shorter tail towards high *B* values for increasing seed field strengths. Summarizing, also in the full physics case the lower intensities of the *B* field are set by the initial seed strength. However, due to the inclusion of baryon physics, the amplification of magnetic field within cosmic structures – in particular at halo centres – reaches saturation and the memory of the initial seed field is lost completely.

Fig. 7 confirms the general trends discussed above. The figure shows two-dimensional histograms of of *B* field intensity versus baryon overdensity at redshift zero for the reference simulations box-512-ad (top row) and box-512-fp (bottom row) as a function of the seed field intensity, growing from left to right as in Fig. 6. The histograms and the overplotted lines are constructed in the same way as in Fig. 4.

In the adiabatic run, it can be seen that the net effect of a change in the seed field strength is to shift vertically the histogram and the associated relations. The shift is given by a factor of 10^2 for each panel from left to right, which is

exactly the variation of the seed field in the three runs. In the simulation featuring the largest seed field at high overdensities the value of the *B* field does not fully grow up to the expected value, suggesting that the amplification process has reached saturation, at least in the most dense regions. Except for that, no other effect is present. In particular, the overdensity range does not vary, which again is consistent with the fact that, for these choices of the magnetic field strength, the magnetic field is dynamically unimportant.

In the full physics run the vertical shift is also present, but it only affects the lower values of the *B* field. The upper values are consistently remaining at the same location, a further indication that saturation has been reached and that the maximum value of the *B* field lost memory of the initial strength from which it started. Not surprisingly, the dynamic range in *B* field intensities shrinks for increasing values of the seed field. Eventually, if the value of the seed field keeps increasing, the upper and lower parts of the diagram will have the tendency to align. If we extrapolate the results from the right-hand panel, the alignment will occur for a critical seed field of $\sim 10^{-8}$ G. It is plausible, however, that either this high intensity of the seed field corresponds to a larger value of the *B* field at saturation or that the *B* field becomes dynamically important, altering dramatically
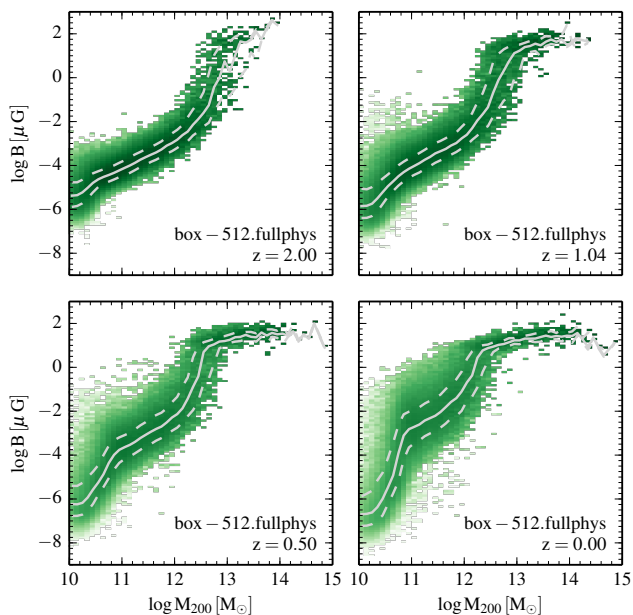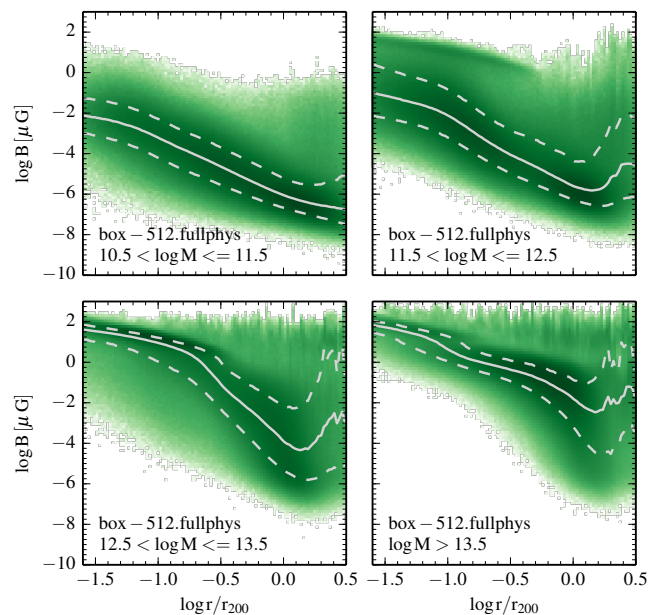
Figure 8. Redshift evolution of the B field intensity versus virial mass (M_{200}) of FOF groups for the simulation box-512-fp. Redshift is indicated on the bottom-right corner of each panel. The panels show two-dimensional histograms colour coded according to the mass of gas falling on to each bin (darker shades correspond to larger masses). Light grey lines represent the median (solid) and the 16th and 84th percentiles (dashed) of the B field distribution as a function of the virial mass. Magnetic field steadily increases with halo mass at all redshifts, forming a well-defined sequence in all the panels. The same trend is present in the corresponding adiabatic simulation (not shown). However, the inclusion of baryon physics makes the relation considerably steeper and allows the B field to reach much larger (up to four orders of magnitude) values.

Figure 9. Magnetic field profiles as a function of distance expressed in terms of the virial radius for the FOF groups of the simulation box-512-fp at redshift zero. The figure has been created by stacking the FOF groups contained in the simulation in four virial mass bins as indicated in the bottom left corner of each panel. The panels show two-dimensional histograms colour coded according to the mass of gas falling on to each bin (darker shades correspond to larger masses). Grey lines represent the median (solid) and the 16th and 84th percentiles (dashed) of the resulting profiles.

structure formation. On the other hand, for a too small value of the seed field it is conceivable that the dynamic range spanned by the magnetic field will not increase indefinitely, but numerical effects such as diffusion on the grid scale (Cho & Ryu 2009; Jones et al. 2011; Ryu et al. 2008; Schekochihin et al. 2004; Vazza et al. 2014) may prevent the final field to grow up to the values reached in the current simulations.

3.3   Magnetic field in haloes

From the previous analysis it is clear that the amplification of the magnetic field is particularly effective within the assembling structures and in the presence of radiative gas cooling and of baryon processes. Therefore, in this section we will be mostly concerned with the box-512-fp simulation that explicitly includes baryon physics (but see Figs 10 and 11). In the adiabatic case, most of the conclusions reached here will hold as well, although the strength of the resulting B fields is much lower, especially in the central regions of haloes. For clarity, with halo scales we indicate distances from the centres of haloes of the order of the virial radius r_{200} determined as the radius enclosing $200\,\rho_{\rm crit}$, the latter being the critical density of the Universe. We will first discuss the

general B field properties of the halo population (Sect. 3.3.1) and then analyse a few individual examples (Sect. 3.3.2).

3.3.1   B field in the halo population

In Fig. 8, we present two-dimensional histograms of B field intensity versus halo virial masses – determined as the total mass enclosed by halo virial radius r_{200} – at different redshifts for the reference run box-512-fp. The colour shading in the histogram represent the gas mass within the virial radius of each identified halo in the simulation box falling on to each bin. We also plot the trends of the 16th, median and 84th percentiles (grey lines).

From the figure it is immediately visible that a well-defined correlation between halo virial masses and intensity of the magnetic field is present at all redshifts, with more massive haloes hosting larger average magnetic fields. This is expected on the basis of the hierarchical bottom-up nature of structure formation in a ΛCDM universe. As small structures merge to form more massive ones, turbulence and shear flows are excited. This in turn promotes the amplification of the magnetic field contained in the merging structures, that was already boosted from its seed value by gravitational gas compression, largely due to effective cooling in the halo central regions, as well as by galactic outflows generated by stellar and black hole (for the larger structures) feedback. Also, additional processes (such as ram-pressure stripping),
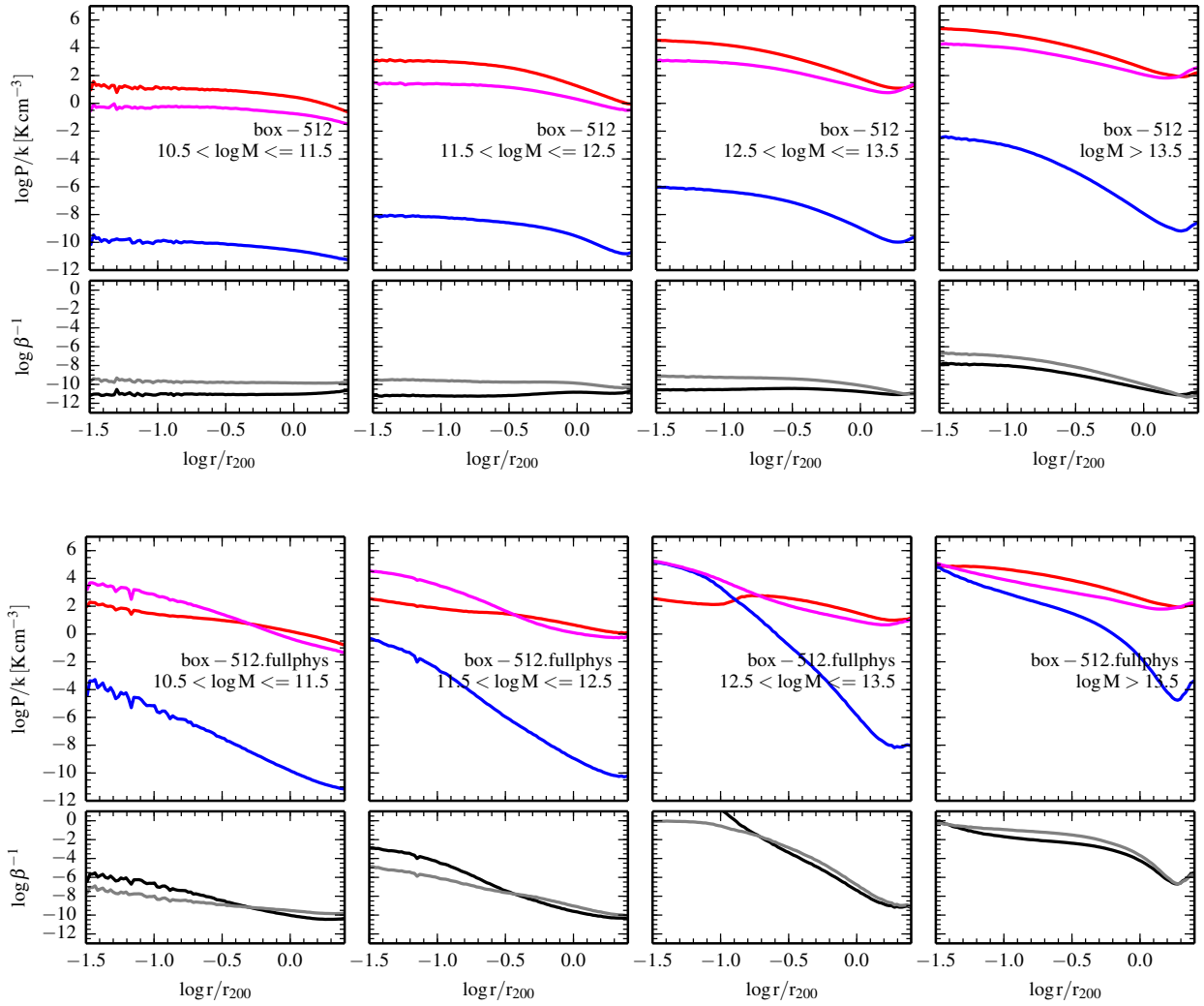
Figure 10. Volume-weighted thermal pressure (red lines), magnetic pressure (blue lines), and kinetic energy density (magenta lines) median profiles as a function of distance expressed in terms of the virial radius for the FOF groups of the simulations box-512-ad (top row) and box-512-fp (bottom row) at redshift zero. The figure has been created by stacking the FOF groups contained in the simulation in four virial mass bins as indicated in each panel. Lines in the bottom panels represent the ratio between magnetic and thermal pressures (black) and between magnetic pressure and kinetic energy density (grey). Magnetic fields are largely subdominant and their contribution to the total pressure of the halo gas is negligible. However, in the box-512-fp simulation, in the mass bin $12.5 < \log M/M_\odot \leq 13.5$ the magnetic field can reach values well above the gas thermal energy but this is limited only to the inner regions $r \lesssim 0.1\,r_{200}$. In the full physics simulations kinetic energy tends to dominate the profiles in the inner regions, except for the most massive mass bin.

could be at work to generate turbulence in massive haloes. Interestingly, the relationship between the halo virial mass and the median intensity of the hosted B field steepens with time. Moreover, at the high-mass end $(M_{200} \gtrsim 10^{13}\,\mathrm{M_\odot})$ the magnetic field intensity reaches a maximum value of $\sim 10 - 30\,\mu\mathrm{G}$. At the low-mass end, instead, there is a hint of decrease of the average field intensity as a function of time, which can be explained by the cosmological expansion (see eq. [2]).

In Fig. 9, we show stacked magnetic field intensity profiles as a function of radius (normalized to the virial radius) at redshift zero for the reference simulation box-512-fp. The stacking of the FOF groups in the simulation has been done for four different virial mass bins, indicated in the bottom-left corner of each panel. The colour shading encodes the

gas mass falling into each bin and the grey lines the 16th, median and 84th percentile of the resulting profiles.

The overall trend, for all mass bins, is that of a declining B field as a function of radius. For low-mass haloes (top-left panel) the decrease has a roughly constant slope. In the centres of these haloes the median magnetic field intensity is $\sim 10^{-2}\,\mu\mathrm{G}$, as compared to a (physical) seed field strength of $10^{-8}\,\mu\mathrm{G}$. In the external regions the median B field is about a factor of 10^5 smaller. For higher mass haloes, the profiles are always declining but in the central regions larger median values of the B field intensity, which saturate at $\sim 10^2\,\mu\mathrm{G}$ for the most massive bins, can be reached. In the outskirts, the amplification of the B field depends on the mass bin considered and it is more efficient the larger the halo mass. This again agrees with the expectations of hierarchical structure growth in which more massive haloes

are more likely to have experienced more frequent merger events. The higher merger frequency triggers gas processes such as turbulent motions responsible for magnetic field amplification, leading to larger B field values. Finally, for the most massive objects also gas stripped from substructures may contribute to increase the B field in the halo.

In Fig. 10, we present volume-weighed magnetic pressure (blue lines), thermal pressure (red lines), and kinetic energy density (magenta lines) median profiles, together with their ratios (black lines for magnetic to thermal and grey lines for magnetic to kinetic), at $z = 0$ for the reference simulations box-512-ad (top row) and box-512-fp (bottom row). The profiles are shown as a function of the distance from the halo centre normalized to the halo virial radius, in analogy with Fig. 9, and in the same halo mass bins.

If we compare the magnetic pressure to the thermal pressure and kinetic energy density profiles, we can immediately see that the magnetic fields are subdominant; i.e. their importance for the dynamics of the system is negligible. The only exception are the two most massive bins of the full physics run, in which the magnetic pressure is comparable to or exceeds the gas thermal pressure and kinetic energy in the inner regions ($r \lesssim 0.1\, r_{200}$). The thermal pressure profiles of both simulations in each mass bin are similar, indicating that the support needed against gravity within haloes is mostly provided by the "standard" gas pressure. Only the $12.5 < \log M/\mathrm{M_\odot} \leq 13.5$ mass bin in the full physics run shows a pressure dip in the central regions, likely due to the efficient radiative cooling of the gas, which can explain why the magnetic contribution to the total gas pressure is so large.

On the other hand, magnetic pressure profiles are very different between the two runs. In the adiabatic case, their shape closely follows that of the thermal gas pressure, as can be seen from the profile of their ratio, which is approximately constant, at a level of 10^{-11}, with radius and among the mass bins, with the exception of the most massive one where a larger deviation from a flat profile can be seen. This tiny value is an additional confirmation of the unimportant role played in the dynamics of the haloes, but it is interesting to note that the absolute value of the magnetic pressure (and thus of the magnetic field intensity) increases for the most massive systems, indicating that the amplification process is more effective in high mass structures, which also feature a larger value of the gas kinetic energy density that can be used to power the amplification of the B field. In the full physics simulation, magnetic pressure profiles show a much steeper decline with respect to their adiabatic counterpart. This is due to the fact that larger values of magnetic field intensities can be reached in the halo centres where cooling and other baryon processes are at work – substantially increasing the gas kinetic energy density, which is indeed the dominant component in the halo inner regions for all the mass bins but the most massive – while the level of amplification outside haloes ($r \gtrsim r_{\mathrm{vir}}$) is lower and similar to that of the adiabatic simulations. As in the adiabatic case, larger values of magnetic pressure are found for larger halo masses.

In Fig. 11, we show the redshift zero average B field as a function of the (mass-weighted) average temperature for haloes more massive than $10^{13.5}\, \mathrm{M_\odot}$ for the simulations box-512-ad (top panel) and box-512-fp (bottom panel). The average values have been computed in a spherical region cen-
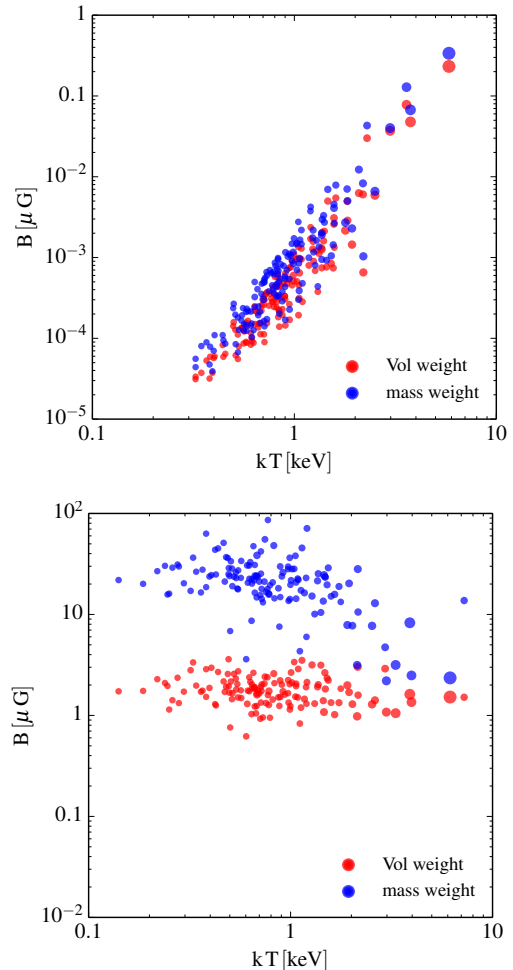
Figure 11. Average volume-weighted (red symbols) and mass-weighted (blue symbols) magnetic field as a function of the mass-weighted gas temperature for the box-512-ad (top panel) and box-512-fp (bottom panel) simulations at redshift zero. The averaging procedure for both temperature and B field has been performed in a region within 35% of the virial radius of each halo. Only haloes more massive than $10^{13.5}\, \mathrm{M_\odot}$ have been considered in this plot. Symbols sizes are scaled according to halo virial masses.

tred on the potential minimum of each halo and of radius equal to $0.35\, r_{200}$. To compute the magnetic field value we adopt both a volume (red symbols) and a mass (blue symbols) weighting procedures, the latter to allow a comparison with a similar figure presented in Donnert et al. (2009) who studied the amplification of B field in cosmological simulations of galaxy cluster formation. Their simulations did not include radiative cooling but focused on a more elaborate way of seeding the primordial magnetic field via ejection of magnetized material by galactic outflows.

In the adiabatic case (top panel) we recover a tight relationship as in Donnert et al. (2009) between the halo central temperature and its mean magnetic field. The weighting procedure adopted for the computation of the B field does not lead to a significant difference in the final derived values, although mass-weighting yields consistently larger values (about a factor of 2) than volume-weighting. The slope of the relationship is approximately $B \propto T^3$ with a hint of
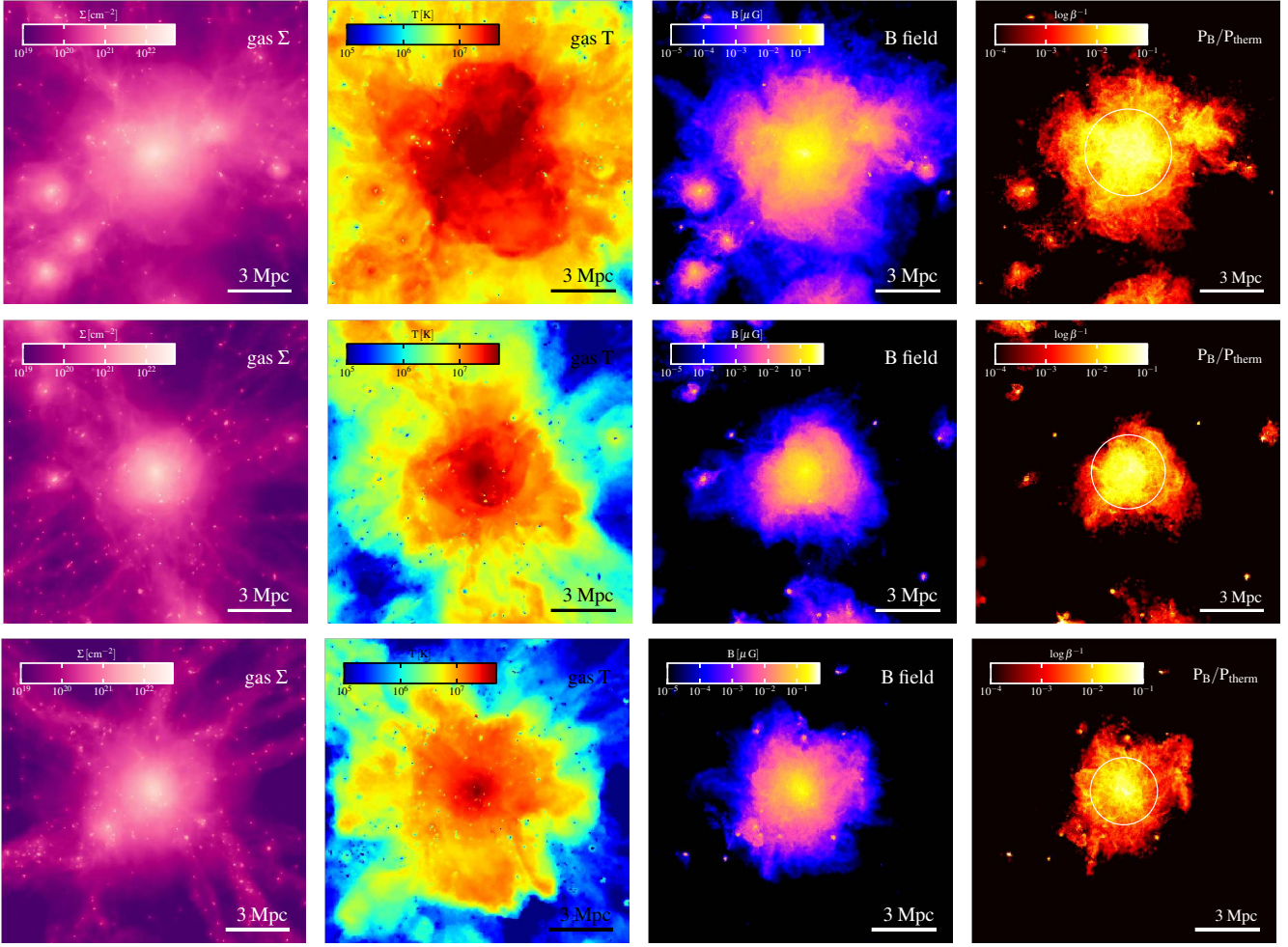
Figure 12. Redshift zero projections of gas density, gas temperature, magnetic field and the ratio between magnetic and thermal pressure (from left to right) for the three most massive haloes in the simulation box-512-fp (ordered by mass from top to bottom). The projection region is a cube of 15 Mpc on a side (in physical units) centred on the halo potential minimum. The white circle in the rightmost panels indicates the virial radius (r_{200}) of each halo.

flattening at the low-temperature end ($\lesssim 1\,\mathrm{keV}$). The most remarkable difference with respect to Donnert et al. (2009) is that the values of the central magnetic field reached in our simulation are lower by about two orders of magnitude. This is due to a combination of causes. For instance, we have chosen a larger radius within which to average the field and this naturally brings down the estimated average value. The most important factor, however, is the intensity of the seed field. We have already shown that in the adiabatic runs this is the crucial quantity that controls the final intensity of the magnetic field. In our fiducial run we chose a seed field of $10^{-14}\,\mathrm{G}$, to be compared to values of $\simeq 10^{-12}\,\mathrm{G}$ in Donnert et al. (2009) simulations. Therefore, according to what discussed in Sect. 3.2, our results must be rescaled by approximately this factor, which will make this discrepancy less severe. Finally, also numerical resolution can play a role in defining the final B field strength.

In the full physics run (bottom panel), the monotonically increasing trend of magnetic field intensity as a function of the temperature is disrupted. This shows the dramatic impact that baryon physics, and especially of outflows originated by galactic winds and AGN feedback, has

on the dynamics of the gas within haloes, which translates in a stark difference in the amplification of the field with respect to the adiabatic run. There is a much larger difference between magnetic field values derived by volume-weighted averages versus mass-weighted ones, with the latter being on average about one order of magnitude larger. This is the consequence of the cell refinement scheme adopted in our calculations that keeps the mass per cell within a factor of 2 from a predefined target. The approximately constant mass per cell implies that cells are given the same weight to compute the average field regardless of their distance. This does not hold anymore when magnetic field intensities are volume weighted. More distant cells, with smaller B fields, have on average larger volume and are given more weight in the averaging procedure, thus reducing the resulting B field strength. The volume-weighted magnetic field strength does not show a large variation with temperature remaining on the level of a few μG. The mass-weighted field declines with temperature reaching $\sim 1\mu$G for the more massive systems. The values of central magnetic fields for the largest systems (up to a few tens of μG) are consistent with observational determinations in galaxy clusters (e.g. Feretti et al. 1995,
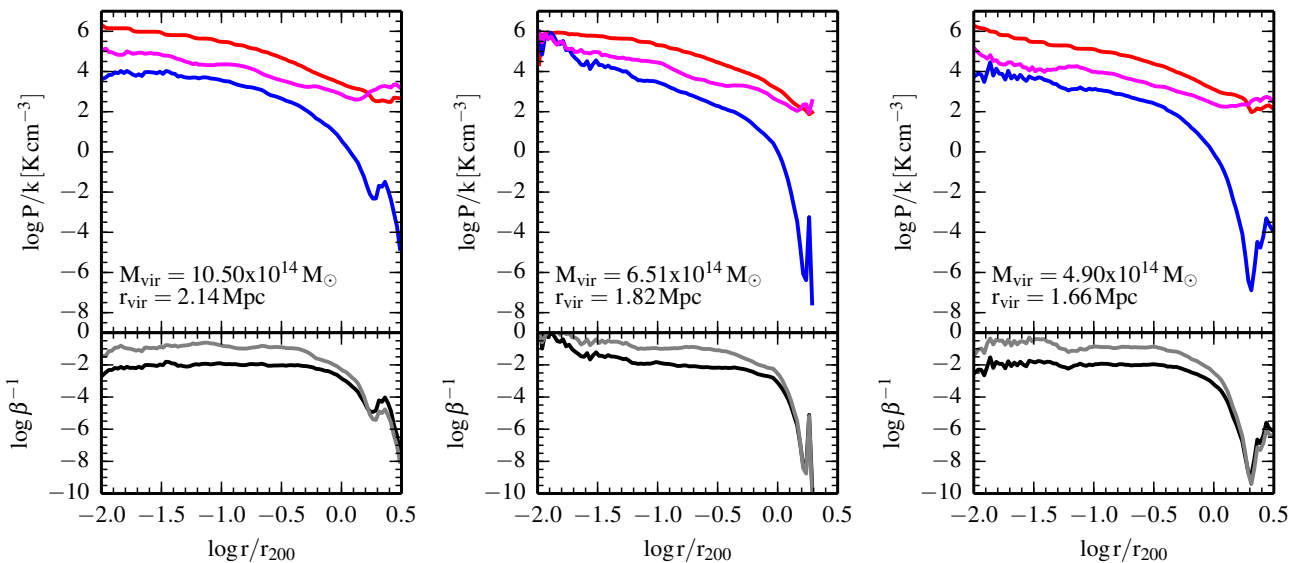
Figure 13. Volume-weighted thermal pressure, magnetic pressure, and kinetic energy density median profiles for the three most massive haloes of simulation box-512-fp. The layout of each panel is the same as in Fig. 10.

1999; Murgia et al. 2004; Guidetti et al. 2008; Govoni et al. 2006; Bonafede et al. 2009, 2011).

3.3.2   B field in individual haloes

To better understand the trends discussed above and to make a closer connection with the observations (see also next section), we now analyse some of the haloes individually by taking the three most massive haloes in the simulation box-512-fp. Fig. 12 presents different projected quantities (gas density and temperature, magnetic field strength and the ratio between magnetic and thermal pressure) at redshift zero. The haloes are ordered according to their virial mass, which covers the range from $4.9 \times 10^{14}\,M_\odot$ to $1.05 \times 10^{15}\,M_\odot$.

These three haloes are representative of large groups or clusters of galaxies. The gas density distributions show that they are almost spherically-symmetric objects. In the outskirts there are still signs of substructure accretion and at large scales filaments of material connect the central virialized object to the cosmic web. The temperature distribution in most cases extends to larger scales than the gas density. A hotter core can be identified closer to the central regions, but high temperatures can also be found beyond the halo virial radius (indicated by the white circles in the rightmost panel). This is a direct consequence of the radio mode AGN feedback model that we have adopted, which is particularly effective in ejecting (hot) gas at large distances from the centre (Genel et al. 2014). The magnetic field closely follows the gas density distribution. It reaches the largest values in the centres of the haloes and then rapidly declines with decreasing gas density. Local increases of the magnetic field can be seen outside the central parts of the haloes in correspondence of density enhancements due to infalling sub-structures. Notwithstanding this close connection between magnetic field and gas properties, and consis-

tently with the results of Fig. 10, magnetic pressure declines more rapidly than gas thermal pressure as it is shown in the rightmost panels. Only inside the halo virial radius the ratios between the two pressures can reach values of a few percent, to rapidly drop to 10^{-4} and below outside a few r_{200}.

This trend is confirmed by Fig. 13, in which we present thermal pressure, magnetic pressure and kinetic energy density profiles for the three haloes. This figure is analogous to Fig. 10, the only difference being that the profiles are not resulting from a stacking but computed individually for each halo. Again we see that the behaviour of the three profiles is very similar. Interestingly, and in contrast to what we have found for smaller haloes (see Fig. 10), the kinetic energy density is in general below the gas thermal pressure, except at distances larger than the virial radius. The ratios between magnetic and thermal pressure (black line) and between magnetic pressure and kinetic energy (grey line) are roughly flat up to the virial radius. The ratio between magnetic and thermal pressure is approximately equal to 10^{-2}, in agreement with galaxy cluster observations (Feretti et al. 1995, 1999; Murgia et al. 2004; Guidetti et al. 2008; Bonafede et al. 2009), intracluster medium heating models (Kunz et al. 2011), and earlier numerical results (Dubois & Teyssier 2008; Bonafede et al. 2011; Ruszkowski et al. 2011; Vazza et al. 2014). The ratio between magnetic pressure and kinetic energy density is larger and in general in the range $\sim 0.1 - 0.4$. We note this range agrees well with numerical work on small-scale dynamos (see e.g. Sur et al. 2012, and references therein). Past the virial radius the magnetic pressure drops abruptly and becomes negligible with respect to the gas thermal pressure and kinetic energy density. Consistent with the results of the previous section, magnetic fields do not play a major role in the dynamics of the gas within these systems.
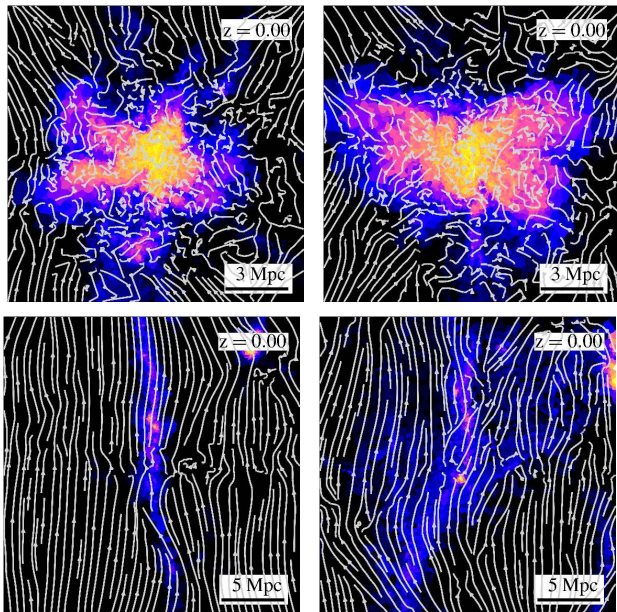
Figure 14. Magnetic field slices at redshift zero for a massive halo (top row) and a filament (bottom row) selected from the simulation box-256-fp. On the left column the slice is displayed on the yz plane while on the right-hand column the xz plane is presented. Colour shades maps the intensity of the magnetic field (the colour scale is the same for all the panels). Field lines, indicating the direction of the magnetic field, are also shown.

To give a better idea of the magnetic field configuration within haloes, we show in Fig. 14 two-dimensional slices of the redshift zero magnetic field strength (colour shades) to which magnetic field lines have been superimposed. We selected the third most massive halo of the simulation box-256-fp (top row) and to highlight the differences with lower overdensity environments we contrast its magnetic field properties with those of a filament taken from the same simulation (bottom row). Slices are repeated twice for each object in the yz (left-hand column) and xz (right-hand column) planes.

It is evident that the magnetic field properties in the two environments are very different. First of all, the magnetic field reaches a greater level of amplification within the halo, while the largest value of the field in the filament is comparable to that found in the halo outskirts (the colour scale is the same for all the panels). Even more remarkable is the difference in the morphology of the B field in the two cases. We start by noting that all the slices show the z-direction, i.e. the initial direction of the seed field. It can be seen that outside of the cluster the magnetic field retains this original direction, while it tends to align along the paths where matter is accreted on to the halo. Inside the halo the orientation of the magnetic field is more chaotic, and its coherence scale is considerably smaller than the typical halo size. This is consistent with the picture that magnetic field amplification is driven by turbulent gas motions – originated by gravitational dynamics and the stirring of gas by galactic and AGN outflows – within collapsed structures. For the filament this turbulent reordering of the magnetic field lines is not present and the magnetic field retains its initial direction, which is also the main direction along which the filament develops. In the regions where the filament deviates from this direction
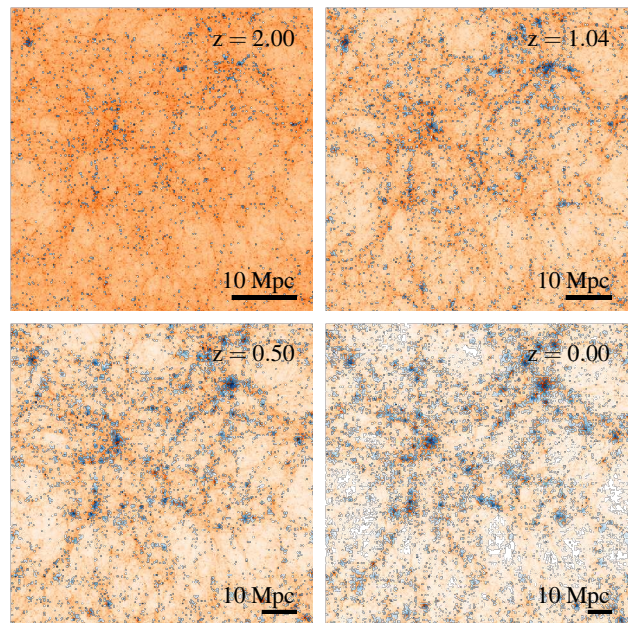

Figure 15. RM map at different redshifts, as indicated in the top right corner of each panel, for the simulation box-512-fp-high. Each panel is 100 h^{-1}Mpc on a side (in comoving units), the full extent of the simulated box. The centre of the projection region corresponds to that of the simulated domain. The plots have been obtained by considering all the gas cells along the z-axis (the initial direction of the seed field) within 25 h^{-1}Mpc (in comoving units) from the centre, for a total thickness of 50 h^{-1}Mpc. The physical scale at the corresponding redshift is indicated on the bottom right corner of each panel. The colour scheme is the same for all the panels and maps logarithmically the absolute value of the RM in the interval $[10^{-6}, 10^2]$ rad m^{-2} in orange shades for (originally) positive values and in blue shades in the opposite case.

also a deviation of the magnetic field is visible. However, the largest component of the magnetic field is always oriented along the z-axis and for scales that can also reach $\sim$ tens of Mpc. In conclusion, even though the initial orientation (and strength) of the seed field is unimportant for the properties of magnetic field within haloes, this orientation is retained on larger scales and in low overdensity regions. We will discuss further this aspect in Sect. 4.

3.4   Faraday RM

A powerful tool to indirectly derive magnetic field strengths comes from the observation of radio sources embedded in or behind massive structures like galaxy clusters. The magnetized plasma within these structures is in fact a birefringent medium. When polarized radiation, such as the linearly polarized synchrotron radiation emitted by a radio source, passes through it, its polarization vector rotates by an amount proportional (through λ^2) to the so-called Faraday rotation measure (RM), defined as

$$\mathrm{RM} = \frac{e^3}{2\pi m_{\mathrm{e}}^2 c^4} \int_0^L n_{\mathrm{e}}(s) B_{\parallel}(s)\, \mathrm{d}s, \qquad (3)$$
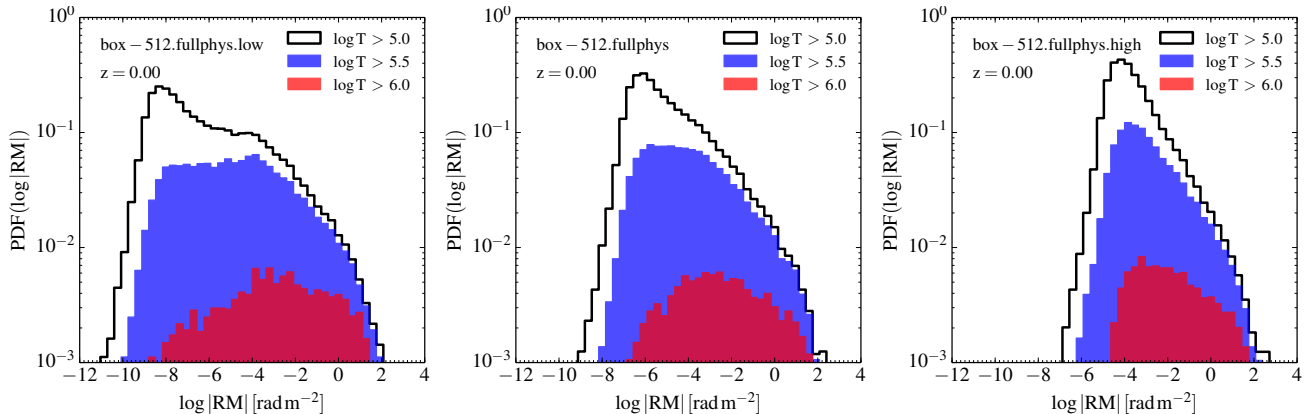
Figure 16. RM PDF at redshift zero for the simulations box-512-fp-low, box-512-fp, and box-512-fp-high (from left to right). The PDFs are calculated for the whole box projecting along the z axis, the initial direction of the B seed field. Colour shades show the contribution to the total PDF (black line), computed for temperatures above 10^5 K, of gas in the temperature ranges indicated in the legend of each panel. Similarly to Fig. 6, increasing the seed field strength shifts the peak of the PDF at low RM values, while leaving the tail at high RM almost unaffected.

where e, m_e and c are the electron charge, electron mass, and speed of light, respectively; n_e is the electron density and $B_\parallel$ is the component of the B field along the line of sight ds. By measuring the shift of the polarization vector at different wavelengths (at least 3 to avoid degeneracies), it is then possible to determine the value of the RM and from it to estimate the magnetic field strength along the line of sight, assuming a distribution for the electron density.

This method is rather indirect and a number of assumptions enter into it in order to obtain the B field strength – which as such can only be considered an average along the line of sight. Nevertheless, comparing the RM predicted by the simulations with the observed values is extremely useful since it can constrain several aspects of our calculations. In particular, we can get further indications about the thermal state of gas in massive structures and the intensity of the magnetic field there, since both the electron density and the magnetic field are present in the definition of the RM (see equation 3). Moreover, RM can also inform on the coherence scale of the magnetic field. Since the RM is an integral quantity, coherent B fields give rise to a strong RM signal, while a more chaotic arrangement of the field weakens the signal because contributions to the path integral tend to cancel out. It is worth noting that some degeneracy between magnetic field coherence and intensity is unavoidable in the final value of the RM: larger but more chaotic B fields can give rise to the same signal of weaker but more ordered field configurations.

In Fig. 15, we present RM measure maps for the simulation box-512-fp-high at different redshifts. The maps have been obtained by projecting along the z-axis (the initial direction of the seed field) the same region as in Fig. 1. The colour scheme is the same in all panels, and maps logarithmically the absolute value of the RM. Since the RM can change sign depending on the predominant direction of the B field we use two different colour shades (orange for positive values and blue for negative ones) to encode this information.

From the figure it can be seen that from a rather homogeneous map at high redshift, the RM signal becomes more and more structured with time. The largest values of

RM tend to follow quite closely the assembly of cosmological structures, and at redshift zero they tend to concentrate on collapsed structures and filaments. The large-scale signal and in particular the contribution from voids declines with time, due to a general decrease of the B field caused by the cosmological expansion. Within collapsed structures, and along the filaments connecting them, positive and negative values of the RM signal co-exist. Since we chose your projection axis to coincide with the initial direction of the seed field, negative RM values signal a field reversals from the original configuration. These reversals are very frequent inside structures where shear flows and turbulence are more effective in amplifying magnetic fields, in agreement with the results discussed in Sect. 3.3.2.

In Fig. 16 we show RM PDFs at redshift zero for different full physics simulations (with resolution 2×512^3) with increasing seed field strengths (from left to right). To generate the PDF the whole computational domain is projected along the z-axis, and only gas with temperature above 10^5 K is considered to exclude the contribution of neutral or partially ionized gas. We also show in each panel the contribution to the total PDF (black lines) of gas with temperatures above $10^{5.5}$ K (blue shades) and 10^6 K (red shades). The PDF is computed for the absolute value of the RM. We explicitly checked that the choice of the projection direction does not alter the properties of the resulting PDFs.

In agreement with the results in Sect. 3.2, changing the intensity of the seed field strongly alters the PDF at lower values of RM. The peak of the PDF is shifted by approximately two orders of magnitude in each panel – the amount by which the seed field is varied. Low values of the RM are found in low-density regions and this indicates that the RM signal in these regions is very sensitive to the initial B field strength. In low-density regions low or little (turbulent) B field amplification, which also set the coherence scale of the field, is expected. Hence, this sensitivity of the PDF to the value of the seed field is ultimately related to the intensity that the magnetic field can attain. We showed earlier that at low baryon overdensities full physics and adiabatic runs
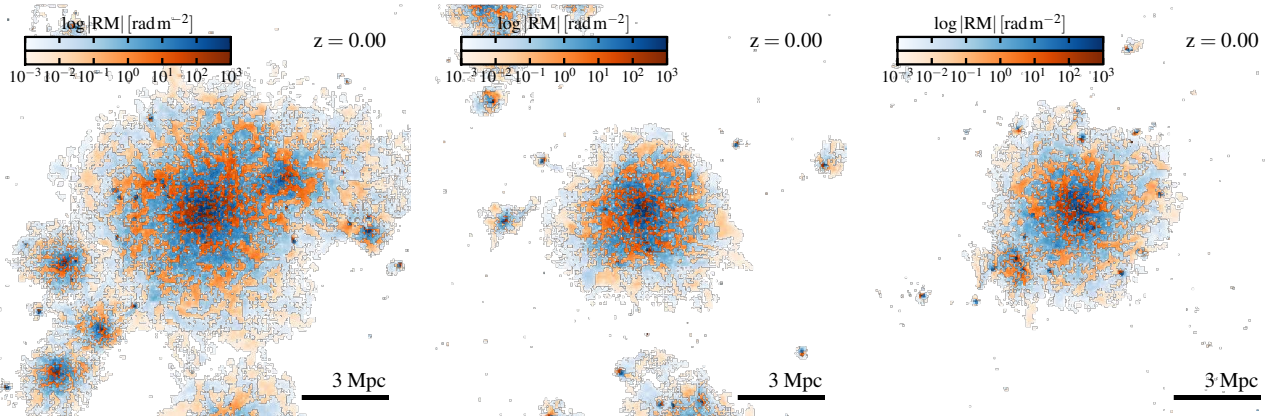
Figure 17. RM maps for the three most massive haloes of simulation box-512-fp. The maps have been calculated for a cubic box of 15 Mpc on a side, centred in the potential minimum of the three haloes. The projection direction corresponds to the z-axis, the initial direction of the magnetic field. Similarly to Fig 15, the colour scales adopt a logarithmic mapping of the absolute value of the RM with orange shades representing positive and blue shades negative values. It is clearly visible the tangled structure of the magnetic field within the haloes due to its turbulent amplification.
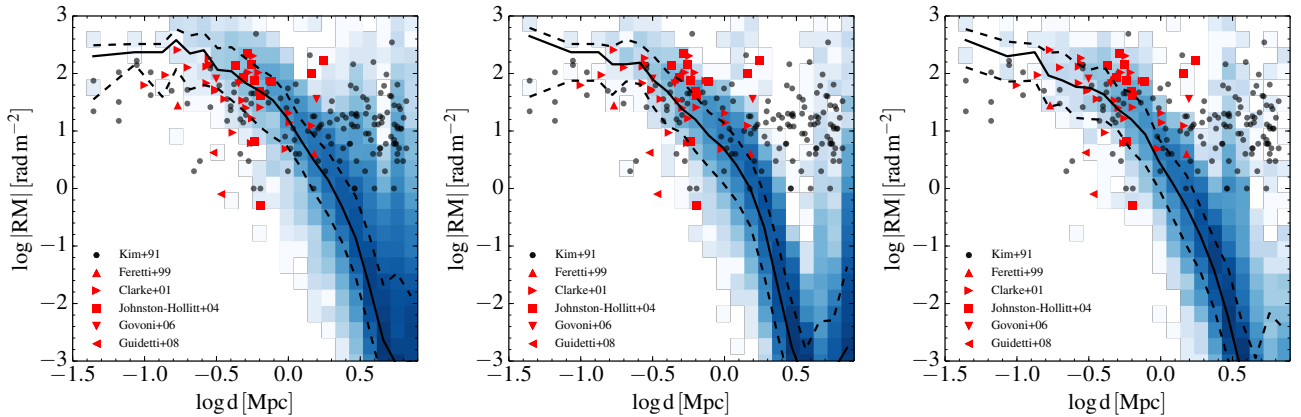
Figure 18. Radial profiles, in terms of the projected distance from the halo potential minimum, of the RM maps in Fig. 17. Colour shades represent the number of pixels falling into each radial and RM bins. Solid black lines indicate the median trend while dashed black lines show the 16th and 84th percentile of the distribution. Coloured symbols are actual measurements of RM in galaxy clusters (references are indicated in the panel legends). It is evident the exponential drop of the RM signal as a function of radius.

have a similar behaviour, and that the intensity of the seed field basically sets the final B field strength.

At the opposite end (i.e. for large RM values) the dependence of PDF on the seed field disappears and the distributions look rather similar. This is again consistent with our earlier findings on the saturation of the amplification of the B field at high baryon overdensities. The maximum value of the RM shows a little residual dependence on the seed field strength, perhaps due to a more coherent field configuration for larger seed field value that slightly increases the RM signal. Temperature seems to play a secondary role for the properties of the RM PDF, but this can be just a reflection of the fact that neutral and partially ionized gas has been excluded from the calculation of the PDFs. Not surprisingly, gas at $T > 10^{5.5}$ K has a broader distribution than gas selected with a larger temperature cut ($T > 10^6$ K). The latter also peaks approximately at $\log |\mathrm{RM}| \sim -3\,\mathrm{rad\,m^{-2}}$ independently of the seed field value, while the peak in the distribution of colder gas (which can be also located in lower

density regions) shifts towards higher RM values with increasing seed field strength.

In Figs 17 and 18 we analyse the RM signal of the three most massive haloes of the simulation box-512-fp (see also Sect. 3.3.2). We start, in Fig. 17, with the Faraday RM maps of the three haloes at redshift zero. The maps have been obtained by integrating along the z-axis equation (3) in a cubic box of 15 Mpc on a side, centred on the haloes potential minimum and aligned with the simulation box. Again, the particular choice of the projection direction leaves essentially unaltered the main features of the maps (see also the top row of Fig. 19). We use the same colour scheme of Fig. 15 and the resulting value of the RM (in $\mathrm{rad\,m^{-2}}$) is indicated on the colour bar on the top-left corner of each panel.

It is clearly visible that the three haloes, although quite different in mass, show rather similar features in their RM measure maps. First of all, RM signal extends roughly in the same region where a significant B field is present (com-

pare the maps with the third column of Fig. 12). This is not surprising since the dependence on the electron density is secondary here (due the high temperature the gas is fully ionized). However, these maps also clearly show the tangled structure of the magnetic field within the haloes as a results of its turbulent amplification. Regions with coherent sign of the RM can be as small as a few pixels (~ 50 kpc at the current map resolution), which is a much lower value than the virial radii of the haloes ($\sim$ few Mpc). Values of the RM as high as 10^3 rad m^{-2} are not uncommon in the halo centres, but the signal declines considerably with radius and drops very rapidly outside the virial radius, closely mimicking the behaviour of the magnetic field. Local enhancements of the RM signal due to infalling substructures are also present.

To study more closely the radial variation of the RM, in Fig. 18 we present radial profiles of the maps above as a function of the projected distance from the halo centre. Colour shading shows the number of pixels falling into each radial and RM bins, while black solid lines show median trends and black dashed lines the 16th and 84th percentiles. Symbols show observed values of RM detected in galaxy clusters (Kim et al. 1991; Feretti et al. 1999; Clarke et al. 2001; Johnston-Hollitt & Ekers 2004; Govoni et al. 2006; Guidetti et al. 2008). As inferred from the maps, RM is a rapidly declining function of distance. From the median relation we can infer that this decline is almost exponential and little signal is left past the halo virial radius. Only for the most massive halo RM bins are significantly populated for $r \gtrsim r_{200}$. A comparison with the observations shows that our simulations predict the correct RM intensity, especially in the halo central regions. However, our predictions are marginally inconsistent with one of the data set (Kim et al. 1991), which features a more extended distribution of RM in the radial direction. Only the most massive halo of the simulation, thanks to the RM signal originating from the prominent substructures that surround the main body of the halo, can partially predict this signal at radial distances comparable to the virial radius and beyond. Note, however, that in the previous analysis we did not include the Galactic and extragalactic foreground contributions to the RM signal. Outside the Galactic plane these contributions can account for $\sim 6-8$ rad m^2 (Schnitzeler 2010), thus rendering the discrepancy between the observed and predicted RM radial profiles less severe.

4 DISCUSSION

An essentially arbitrary aspect in cosmological ideal MHD simulations is represented by the freedom in the choice of the initial seed field. The chosen initial field configuration must be divergence free, but except for this requirement only scant and somewhat uncertain observational constraints on the magnetic field strength are currently available in very low density environments or at high redshift (Neronov & Vovk 2010; Planck Collaboration XIX 2015). Also, theoretical models of cosmic magnetogenesis come in a variety of flavours with different predictions for both the intensity and the configuration of primordial fields (see Widrow et al. 2012, and references therein). Numerical simulations can potentially exploit this freedom to constrain theoretical models by testing their predictions for the resulting magnetic field

properties at large baryon overdensities, where observational limits are more stringent and abundant.

In our simulations we have chosen the simplest divergence-free field configuration: a uniform magnetic field oriented along the z-axis of the simulation box. We have extensively discussed how the strength of the magnetic seed field influences the results of non-radiative and full physics runs. We concluded that, while in non-radiative runs the seed field intensity provides an overall normalization factor to the values of the final magnetic field strength, in full physics runs magnetic field within structures always reached roughly the same maximum value *regardless* of the initial seed field, whose strength is consistent with the observational constraints cited above. The magnetic field loses memory of its initial configuration even for large seed field variations (see also Pakmor et al. 2014). Although this is desirable feature from a numerical modelling point of view, because results are independent of the particular choice of the seed field, it makes simulations a less stringent test for cosmic magnetogenesis models. Different authors, using different numerical techniques, baryon physics prescriptions and seeding strategies find similar results (e.g Dolag et al. 1999; Donnert et al. 2009; Xu et al. 2010). The situation is more promising in less dense regions such as filaments and voids, where the dependence on seed field is stronger, and allows us to discriminate among different scenarios (Ryu et al. 1998; Donnert et al. 2009; Dubois & Teyssier 2010; Akahori & Ryu 2011; Akahori et al. 2014). However, we stress again that numerical simulations are confronted here with the scarcity of data although this will improve with the current and forthcoming generation of radio instruments, such as LOFAR and SKA, which are potentially able to detect magnetic fields of the order of 1 nG or below (Beck 2007a; Pritchard et al. 2015; Sethi & Subramanian 2009; Vazza et al. 2015a).

As an example of how low density environments retain a stronger imprint of the initial magnetic seed field, we repeat in Fig. 19 the analysis carried out in Fig. 14. We present two-dimensional slices of the redshift zero magnetic field and its orientation on the yz plane, but for a seed field with initial direction along the z-axis (left-hand column) and the y-axis (right-hand column), respectively. The slices corresponding to the same object are centred at exactly the same point for both field directions. Hence, as all the other parameters are not varied between simulations, the differences in magnetic field strength and orientation are due only to the different choice of the initial direction of the seed field.

The agreement between the magnetic field intensities in the two runs is very good. In the halo, the maximum strength reached by both simulations is essentially the same and also the characteristic tangled orientation of the field is present. Minor differences are also visible, as for instance a more developed magnetic filament in the upper-right part of the halo in the case of the y-axis oriented seed field or a larger magnetized substructure in the lower region for the simulation with the default magnetic field orientation. Also, the magnetic field in the halo appears to be more extended in the y-direction in the latter case. The most striking difference, however, is in the orientation of the field just outside the halo, which is strongly aligned with the seed field initial direction in regions where matter accretes on to the virialized structure as well.

The effect is even stronger for the filament. Here, the
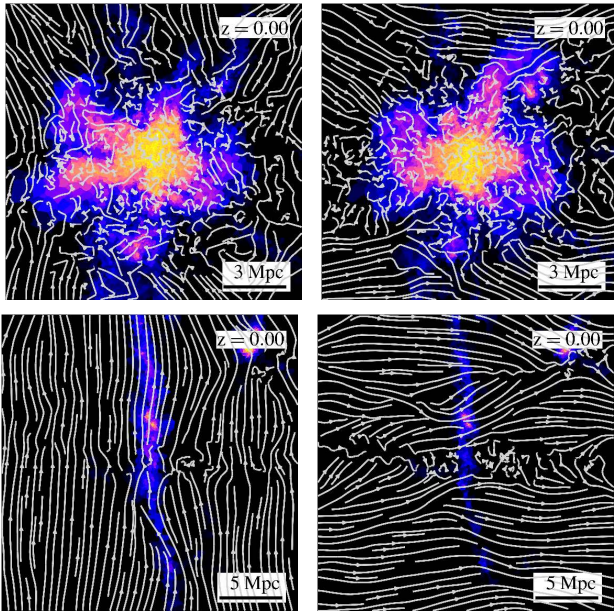
Figure 19. The same as Fig. 14, but showing the simulation box-256-fp with seed field oriented along the z-axis (left-hand column), and the simulation box-256-fp-ydir with exactly the same set up but seed field aligned with the y-axis (right-hand column). For all the slices only the yz plane is displayed.

prevailing direction of the B field is that of the initial seed, as field lines flip by 90° between panels. The magnetized structure in the upper-right corner looks very similar in both cases, while the filament, although conserving the overall shape, shows a larger magnetization for the default B field orientation. This is because the magnetic field amplification is the result of gas compression in the filament, which mostly occurs perpendicularly to the filament itself. In default magnetic field orientation field lines are perpendicular to the motion of gas and are thus dragged along with it. This dragging results in a stronger amplification effect than in the other simulation where one of the gas velocity component is aligned with the magnetic field lines which, as a result, are compressed to a lesser degree. The final maximum B field strength in the filament is $\sim 1\,\mathrm{nG}$ for the default orientation of the seed field, and about a factor of 3 less for the y-axis orientation. These results are in agreement with Brüggen et al. (2005) and Vazza et al. (2014) findings[3], and about a factor of 10 smaller than the values quoted by Akahori & Ryu (2010), Akahori & Ryu (2011), and Ryu et al. (2010), who however did not follow the field evolution self-consistently in their cosmological simulations but used a prescription to estimate the strength of the magnetic field based on MHD turbulence simulations. Note that at filament overdensities, our simulations are still sensitive to the value of the initial seed field. Thus, the discrepancy with simulations predicting higher B field intensities can be reconciled by choosing a larger initial seed field.

[3] Vazza et al. (2014) used a seed field strength 10^4 larger than our default choice, but also the more diffusive HLL (Harten et al. 1983) Riemann solver that could have in principle reduced the B field amplification.

We conclude that our general results are robust with respect to both the orientation and the strength of the adopted seed field. However, a more detailed level of analysis reveals some subtle differences in the evolution of the properties of the magnetic field, especially in low-density environments. Also, the choice of a uniform seed field implies that the field structure in underdense regions of the Universe is coherent on large spatial scales and it is unclear whether this is an accurate description of primordial cosmological magnetic fields (Beck et al. 2013a; Cho 2014; Kronberg et al. 1999; Kulsrud et al. 1997; Schlickeiser 2012; Tsagas 2014).

Another important aspect of our simulations for magnetic field amplification is their resolution. We have stressed in many places that, in addition to the gas compression provided by gravitational collapse, shear and turbulent motions of the gas are equally if not more important for the final amplification level reached by the magnetic field. Even at the highest level of resolution, our simulations contain a much lower number of resolution elements than cosmological simulation presented in Vazza et al. (2014). These authors find that in order to develop a small-scale dynamo in cosmological simulations a minimum spatial resolution, depending on the size of the simulated halo, must be achieved (for a $10^{14}\,\mathrm{M}_\odot$ halo the minimum spatial resolution is $\sim 10\,\mathrm{kpc}$). While their results may have been affected by the choice of a relative diffusive Riemann solver, this resolution requirement to capture (small-scale) MHD turbulence remains an important point. We note that we indeed observe a variation in the final strength of the magnetic field as a function of the resolution for halo masses below $10^{13}\,\mathrm{M}_\odot$, especially in the central regions. The discrepancy is less severe for larger haloes. Also, non-radiative simulations show that the degree of amplification of the magnetic field at large baryon overdensity is affected by resolution as well, while the effect is less prominent in the full physics runs. We believe that this is exactly the effect that Vazza et al. (2014) inferred from their simulations.

However, we would like to point out that it is difficult to do a straightforward comparison between the maximum resolution achieved in our calculations and those in a fixed-grid setup as in Vazza et al. (2014). The quasi-Lagrangian nature of AREPO, and its default refinement scheme that keeps the mass per cell roughly constant, naturally leads to a configuration in which the bulk of the resolution elements is put in the most dense regions (i.e. the halo centres), which thus are better resolved than the lower density ones. This automatic adaptive resolution allows us to follow more faithfully the clustering of matter into cosmological structures, but it might not be the optimal choice to capture all the thermal and dynamical processes occurring in gaseous haloes (Nelson et al. 2015). This degradation of the (spatial) resolution of our simulation at large distances from the halo centres, might be the reason for the steep decline of the RM signal in the haloes examined in Fig. 18. Simulations with better resolution throughout the halo are needed to fully prove this point, but the fact that in lower resolution runs the decline of the RM profiles is slightly faster can be taken as an indication that properly capturing the small-scale MHD turbulence is a crucial factor to get the correct level of amplification of the B field (see also Federrath et al. 2011).

Finally, we would like to mention that in our numerical setup AGN feedback, and in particular the radio mode chan-

nel (see Vogelsberger et al. 2013), does not provide a source term of magnetic field for the gas in the haloes of massive objects. Therefore, our simulations are currently neglecting a potential channel to seed a large fraction of the IGM (on the Mpc scale) and filaments with magnetic fields that are stronger than the primordial values during the quasar era at $z \sim 2 - 3$ (Gopal-Krishna & Wiita 2001; Mocz et al. 2011), which could alleviate the tension between the observed and the simulated values of the RM at large radii in massive haloes.

5 SUMMARY AND CONCLUSIONS

We have analysed the properties of magnetic fields in uniformly sampled cosmological box simulations performed with the moving-mesh code AREPO. Our analysis is based on a set of simulations that include magnetic fields in the ideal MHD approximation. The magnetic field is introduced at the beginning of the simulations as a uniform seed field that is subsequently amplified by the formation of cosmological structures. We contrast the final magnetic field properties in two main types of simulations: adiabatic runs including only non-radiative (magneto)hydrodynamics, and full physics runs featuring the fiducial model of baryon physics used in the recent ILLUSTRIS simulation suite. We repeat both adiabatic and full physics simulations at different resolution levels and by varying the strength and direction of the initial seed field in order to assess their importance for the final B field properties. Our main results are as follows.

(i) The intensity of the magnetic field in both adiabatic and full physics runs traces very well the underlying distribution of matter, indicating a close connection between the amplification mechanism of the field and the formation of structures in the Universe.

(ii) The amplification of magnetic field intensity in non-radiative runs is well described by magnetic flux conservation ($B \propto \rho^{2/3}$) at low baryon overdensities. Within collapsed structures magnetic flux conservation under-predicts the magnetic field strength indicating that additional amplification takes place thanks to gas turbulent motions and shear flows.

(iii) In the full physics simulations, B field amplification reaches saturation in collapsed structure. Magnetic field intensities are much larger (up to a factor 10^3) with respect to non-radiative runs. Such a large degree of amplification is attained due to radiative cooling leading to high baryon overdensities and the increased level of turbulent and shear gas motions triggered by galactic outflows and AGN feedback.

(iv) Varying the strength of the initial seed field (up to four orders of magnitude) does not affect the B field saturation value inside haloes in full physics runs. On the other hand, in adiabatic runs the initial seed feed strength provides an overall normalization factor for magnetic field intensities at all overdensities. The same holds for full physics runs at low overdensities.

(v) The initial direction of the seed field does not play any role for the average B field properties and for its orientation inside haloes, since turbulent gas motions rapidly delete any memory of the initial direction. However, the original field orientation is retained in low overdensity environments such as filaments and voids.

(vi) The average B field intensity correlates well with intrinsic halo properties such as viral masses. The introduction of baryon physics (cooling and feedback processes) may disrupt trends that are present in non-radiative runs as, for instance, the B field temperature relation in massive haloes.

(vii) Even in the full physics runs, magnetic fields are subdominant as far as the global gas dynamics is concerned. The ratio between magnetic field and gas thermal pressures is in the vast majority of cases well below the percent level. Only in one of the examined halo mass bins for the (reference) full physics simulation the value of the magnetic pressure is larger than its thermal counterpart. The ratio between magnetic and gas kinetic energy agrees well with what found in small-scale dynamo studies.

(viii) B field values predicted in full physics simulations in the centres of massive haloes span a range from a few up to tens of μG, in agreement with observations of galaxy cluster.

(ix) The predicted Faraday RM signal for the three most massive haloes of the fiducial full physics simulation matches quite well galaxy cluster constraints. However, at radii comparable to the virial radius the inferred RM profiles decline more rapidly than the observational findings.

For the first time, our simulations include magnetic fields within a comprehensive model of galaxy formation physics in large-scale cosmological simulations. This allows us to study the co-evolution of magnetic fields and galaxies on different scales, a possibility that we will further exploit in future work.

REFERENCES

Akahori T., Ryu D., 2010, ApJ, 723, 476
Akahori T., Ryu D., 2011, ApJ, 738, 134
Akahori T., Gaensler B. M., Ryu D., 2014, ApJ, 790, 123
Arshakian T. G., Beck R., Krause M., Sokoloff D., 2009, A&A, 494, 21
Athreya R. M., Kapahi V. K., McCarthy P. J., van Breugel W., 1998, A&A, 329, 809
Balbus S. A., 2003, ARA&A, 41, 555

Barnes J., Hut P., 1986, Nature, 324, 446

Basu A., Roy S., 2013, MNRAS, 433, 1675

Beck R., 2007a, Advances in Radio Science, 5, 399

Beck R., 2007b, A&A, 470, 539

Beck R., Wielebinski R., 2013, Planets, Stars and Stellar Systems. Springer, Dordrecht, p. 641

Beck R., Brandenburg A., Moss D., Shukurov A., Sokoloff D., 1996, ARA&A, 34, 155

Beck R., Fletcher A., Shukurov A., Snodin A., Sokoloff D. D., Ehle M., Moss D., Shoutenkov V., 2005, A&A, 444, 739

Beck A. M., Lesch H., Dolag K., Kotarba H., Geng A., Stasyszyn F. A., 2012, MNRAS, 422, 2152

Beck A. M., Hanasz M., Lesch H., Remus R.-S., Stasyszyn F. A., 2013a, MNRAS, 429, L60

Beck A. M., Dolag K., Lesch H., Kronberg P. P., 2013b, MNRAS, 435, 3575

Berkhuijsen E. M., Beck R., Hoernes P., 2003, A&A, 398, 937

Bernet M. L., Miniati F., Lilly S. J., Kronberg P. P., Dessauges-Zavadsky M., 2008, Nature, 454, 302

Biermann L., 1950, Zeitschrift Naturforschung Teil A, 5, 65

Blandford R. D., Znajek R. L., 1977, MNRAS, 179, 433

Bonafede A., et al., 2009, A&A, 503, 707

Bonafede A., Dolag K., Stasyszyn F., Murante G., Borgani S., 2011, MNRAS, 418, 2234

Boulares A., Cox D. P., 1990, ApJ, 365, 544

Broderick A. E., Chang P., Pfrommer C., 2012, ApJ, 752, 22

Brüggen M., Ruszkowski M., Simionescu A., Hoeft M., Dalla Vecchia C., 2005, ApJ, 631, L21

Carilli C. L., Taylor G. B., 2002, ARA&A, 40, 319

Cho J., 2014, ApJ, 797, 133

Cho J., Ryu D., 2009, ApJ, 705, L90

Clarke T. E., Kronberg P. P., Böhringer H., 2001, ApJ, 547, L111

Cox D. P., 2005, ARA&A, 43, 337

Daly R. A., Loeb A., 1990, ApJ, 364, 451

Dolag K., Stasyszyn F., 2009, MNRAS, 398, 1678

Dolag K., Bartelmann M., Lesch H., 1999, A&A, 348, 351

Donnert J., Dolag K., Lesch H., Müller E., 2009, MNRAS, 392, 1008

Dubois Y., Teyssier R., 2008, A&A, 482, L13

Dubois Y., Teyssier R., 2010, A&A, 523, A72

Ensslin T. A., Biermann P. L., Kronberg P. P., Wu X.-P., 1997, ApJ, 477, 560

Federrath C., Sur S., Schleicher D. R. G., Banerjee R., Klessen R. S., 2011, ApJ, 731, 62

Feretti L., Dallacasa D., Giovannini G., Tagliani A., 1995, A&A, 302, 680

Feretti L., Dallacasa D., Govoni F., Giovannini G., Taylor G. B., Klein U., 1999, A&A, 344, 472

Feretti L., Giovannini G., Govoni F., Murgia M., 2012, A&ARv, 20, 54

Fermi E., 1949, Physical Review, 75, 1169

Ferrari C., Govoni F., Schindler S., Bykov A. M., Rephaeli Y., 2008, Space Sci. Rev., 134, 93

Ferrière K. M., 2001, Reviews of Modern Physics, 73, 1031

Fletcher A., Beck R., Shukurov A., Berkhuijsen E. M., Horellou C., 2011, MNRAS, 412, 2396

Furlanetto S. R., Loeb A., 2001, ApJ, 556, 619

Genel S., et al., 2014, MNRAS, 445, 175

Gnedin N. Y., Ferrara A., Zweibel E. G., 2000, ApJ, 539, 505

Gopal-Krishna Wiita P. J., 2001, ApJ, 560, L115

Govoni F., Murgia M., Feretti L., Giovannini G., Dolag K., Taylor G. B., 2006, A&A, 460, 425

Guidetti D., Murgia M., Govoni F., Parma P., Gregorini L., de Ruiter H. R., Cameron R. A., Fanti R., 2008, A&A, 483, 699

Hahn O., Abel T., 2011, MNRAS, 415, 2101

Hanasz M., Kowal G., Otmianowska-Mazur K., Lesch H., 2004, ApJ, 605, L33

Hanasz M., Wóltański D., Kowalik K., 2009, ApJ, 706, L155

Harten A., Lax P. D., van Leer B., 1983, SIAM Rev., 5, 1

Hopkins P. F., Raives M. J., 2015, preprint, (arXiv:1505.02783)

Hunter J. D., 2007, Computing In Science & Engineering, 9, 90

Johnston-Hollitt M., Ekers R. D., 2004, preprint, (arXiv:astro-ph/0411045)

Jones T. W., Porter D. H., Ryu D., Cho J., 2011, preprint, (arXiv:1108.1369)

Kim K.-T., Tribble P. C., Kronberg P. P., 1991, ApJ, 379, 80

Kotarba H., Lesch H., Dolag K., Naab T., Johansson P. H., Stasyszyn F. A., 2009, MNRAS, 397, 733

Kotera K., Olinto A. V., 2011, ARA&A, 49, 119

Kronberg P. P., Perry J. J., Zukowski E. L. H., 1992, ApJ, 387, 528

Kronberg P. P., Lesch H., Hopp U., 1999, ApJ, 511, 56

Kulsrud R. M., Cen R., Ostriker J. P., Ryu D., 1997, ApJ, 480, 481

Kunz M. W., Schekochihin A. A., Cowley S. C., Binney J. J., Sanders J. S., 2011, MNRAS, 410, 2446

Lewis A., Bridle S., 2002, Phys. Rev., D66, 103511

Marinacci F., Pakmor R., Springel V., 2014a, MNRAS, 437, 1750

Marinacci F., Pakmor R., Springel V., Simpson C. M., 2014b, MNRAS, 442, 3745

Miyoshi T., Kusano K., 2005, Journal of Computational Physics, 208, 315

Mocz P., Fabian A. C., Blundell K. M., 2011, MNRAS, 413, 1107

Mocz P., Vogelsberger M., Hernquist L., 2014, MNRAS, 442, 43

Murgia M., Govoni F., Feretti L., Giovannini G., Dallacasa D., Fanti R., Taylor G. B., Dolag K., 2004, A&A, 424, 429

Nelson D., Genel S., Pillepich A., Vogelsberger M., Springel V., Hernquist L., 2015, preprint, (arXiv:1503.02665)

Neronov A., Vovk I., 2010, Science, 328, 73

Pakmor R., Springel V., 2013, MNRAS, 432, 176

Pakmor R., Marinacci F., Springel V., 2014, ApJ, 783, L20

Planck Collaboration XIX 2015, preprint, (arXiv:1502.01594)

Powell K. G., Roe P. L., Linde T. J., Gombosi T. I., De Zeeuw D. L., 1999, Journal of Computational Physics, 154, 284

Pritchard J., et al., 2015, preprint, (arXiv:1501.04291)

Pudritz R. E., Silk J., 1989, ApJ, 342, 650

Ruderman M. A., Sutherland P. G., 1975, ApJ, 196, 51

Ruszkowski M., Lee D., Brüggen M., Parrish I., Oh S. P., 2011, ApJ, 740, 81

Ryu D., Kang H., Biermann P. L., 1998, A&A, 335, 19

Ryu D., Kang H., Cho J., Das S., 2008, Science, 320, 909

Ryu D., Das S., Kang H., 2010, ApJ, 710, 1422

Schekochihin A. A., Cowley S. C., Taylor S. F., Maron J. L., McWilliams J. C., 2004, ApJ, 612, 276

Schleicher D. R. G., Banerjee R., Sur S., Arshakian T. G., Klessen R. S., Beck R., Spaans M., 2010, A&A, 522, A115

Schleicher D. R. G., et al., 2013, Astronomische Nachrichten, 334, 531

Schlickeiser R., 2012, Physical Review Letters, 109, 261101

Schnitzeler D. H. F. M., 2010, MNRAS, 409, L99

Schober J., Schleicher D., Federrath C., Glover S., Klessen R. S., Banerjee R., 2012, ApJ, 754, 99

Schober J., Schleicher D. R. G., Klessen R. S., 2013, A&A, 560, A87

Sethi S. K., Subramanian K., 2009, J. Cosmology Astropart. Phys., 11, 21

Spergel D. N., Flauger R., Hložek R., 2015, Phys. Rev. D, 91, 023518

Springel V., 2005, MNRAS, 364, 1105

Springel V., 2010, MNRAS, 401, 791

Sur S., Schleicher D. R. G., Banerjee R., Federrath C., Klessen R. S., 2010, ApJ, 721, L134

Sur S., Federrath C., Schleicher D. R. G., Banerjee R., Klessen R. S., 2012, MNRAS, 423, 3148

Toro E. F., 1999, Riemann Solvers and Numerical Methods for Fluid Dynamics: A Practical Introduction. Springer-Verlag

Tsagas C. G., 2014, preprint, (arXiv:1412.4806)

Urry C. M., Padovani P., 1995, PASP, 107, 803

Vallée J. P., 1998, Fundamentals Cosmic Phys., 19, 319

Vazza F., Brüggen M., Gheller C., Wang P., 2014, MNRAS, 445, 3706

Vazza F., Ferrari C., Bonafede A., Brüggen M., Gheller C., Braun R., Brown S., 2015a, preprint, (arXiv:1501.00315)

Vazza F., Ferrari C., Brüggen M., Bonafede A., Gheller C., Wang P., 2015b, A&A, 580, A119

Vogelsberger M., Genel S., Sijacki D., Torrey P., Springel V., Hernquist L., 2013, MNRAS, 436, 3031

Vogelsberger M., et al., 2014a, MNRAS, 444, 1518

Vogelsberger M., et al., 2014b, Nature, 509, 177

Völk H. J., Atoyan A. M., 2000, ApJ, 541, 88

Wang P., Abel T., 2009, ApJ, 696, 96

Widrow L. M., Ryu D., Schleicher D. R. G., Subramanian K., Tsagas C. G., Treumann R. A., 2012, Space Sci. Rev., 166, 37

Xu H., Li H., Collins D. C., Li S., Norman M. L., 2010, ApJ, 725, 2152